



5-2019

A Monolithic Gm-C Filter based Very Low Power, Programmable, and Multi-Channel Harmonic Discrimination System using Analog Signal Processing

Gavin Benjamin Long
University of Tennessee, glong4@vols.utk.edu

Follow this and additional works at: https://trace.tennessee.edu/utk_gradthes

Recommended Citation

Long, Gavin Benjamin, "A Monolithic Gm-C Filter based Very Low Power, Programmable, and Multi-Channel Harmonic Discrimination System using Analog Signal Processing. " Master's Thesis, University of Tennessee, 2019.
https://trace.tennessee.edu/utk_gradthes/5481

This Thesis is brought to you for free and open access by the Graduate School at TRACE: Tennessee Research and Creative Exchange. It has been accepted for inclusion in Masters Theses by an authorized administrator of TRACE: Tennessee Research and Creative Exchange. For more information, please contact trace@utk.edu.

To the Graduate Council:

I am submitting herewith a thesis written by Gavin Benjamin Long entitled "A Monolithic Gm-C Filter based Very Low Power, Programmable, and Multi-Channel Harmonic Discrimination System using Analog Signal Processing." I have examined the final electronic copy of this thesis for form and content and recommend that it be accepted in partial fulfillment of the requirements for the degree of Master of Science, with a major in Electrical Engineering.

Benjamin J. Blalock, Major Professor

We have read this thesis and recommend its acceptance:

M. Nance Ericson, Charles L. Britton, Syed K. Islam

Accepted for the Council:

Dixie L. Thompson

Vice Provost and Dean of the Graduate School

(Original signatures are on file with official student records.)

**A Monolithic Gm-C Filter based Very Low Power,
Programmable, and Multi-Channel Harmonic
Discrimination System using Analog Signal
Processing**

A Thesis Presented for the
Master of Science
Degree
The University of Tennessee, Knoxville

Gavin Benjamin Long
May 2019

Copyright © 2019 by Gavin Benjamin Long
All rights reserved.

ACKNOWLEDGEMENTS

I am honored for the opportunity of working with Dr. Blalock, Dr. Britton, and Dr. Ericson. Their expert experience, continual support, and sincere interest in my success have been highly appreciated during my graduate studies. The personal knowledge I have gained from them will be invaluable to my career as an engineer. Yet, their genuine character and vibrant personality have been a great joy of mine and will continue to influence me during my lifetime.

I'm thankful for the life-long support of my parents, Todd and Betsy Long. They have always encouraged and challenged me to reach my full potential from a young age. With their love and support, I have overcome many obstacles with a bright future ahead, which I owe humbly to them.

I would like to thank my fiancé Varisara for her loving support and understanding when the days were long and the nights were short. Your love, encouragement, and patience have been indispensable during our struggles of graduate school.

I'd also like to thank my ICASL colleagues who have been both a forum of knowledge and a team of support. I owe much appreciation to both Jordan Sangid and Spencer Raby for their contributions toward on the MISA project and my research. Special thanks to Justine Valka, whose measurement data collection and hard work have been a necessity for both my success and the project.

ABSTRACT

A highly selective monolithic band-pass filter with programmable characteristics at micro-power operation is presented. Very low power signal processing is of great interest in wireless sensing and Internet-of-Things applications. This filter enables long-term battery powered operation of a highly selective harmonic signal discriminator for an analog signal processing system. The Gm-C biquadratic circuits were fabricated in a 0.18- μm [micrometer] CMOS process. Each 2nd-order biquad filter nominally consumes 20 μW [microwatt] and can be programmed for the desired gain ($0\text{db}\pm 3\text{dB}$), quality factor (5 to 20), and center-frequency from 1kHz to 100kHz. The 8th-order filter channel achieved an effective quality factor of 30 at 100kHz with an overall power consumption of 108 μW .

TABLE OF CONTENTS

Chapter One Introduction.....	1
Motivation	1
Objective	1
Chapter Two Background	3
Previous Work.....	3
Results.....	4
Improvements	8
Literature Review	11
References on Filters.....	11
Chapter Three Design Development.....	13
Specifications and Requirements	13
Filter Characteristics	13
Design Methodology.....	14
System Architecture.....	14
Behavioral Modeling for High-Level Design	15
Circuit Topologies	19
Technology Current Extraction	21
Simulation	22
Operational Transconductance Amplifier	22
Biquad Filter Cell Optimization.....	26
Bias and Buffer Verification.....	32
System Verification	37
Physical Layout Design	38
Floorplan.....	39
Matching Requirements	40
Chapter Four Test Results	42
Evaluation	42
Testing Plan.....	43
Printed Circuit Board.....	44
Equipment.....	46
Measurements.....	47
Filter Response.....	47
Spectral Sweep.....	50
Power Consumption	54
Harmonic Distortion Analysis	55
Linear Range	57
Matching Performance.....	59
Chapter Five Conclusions.....	70
Summary of Performance	70
Discussion.....	70
Future Work.....	71

List of References	72
Vita.....	76

LIST OF TABLES

Table 1: Power Consumption of Biquad Filters across Frequency Spectrum	54
Table 2: MISA1 Minch Current Mirror Measured Mismatch	60
Table 3: MISA2 Minch Current Mirror Measured Mismatch	60

LIST OF FIGURES

Figure 1: Schematic and Transfer Function of the 2nd-Order OTA-C4 Filter (MISA1)	4
Figure 2: MISA1 16 th -Order Response at 6kHz and Multiple Harmonic Frequencies	6
Figure 3: MISA1 Demonstration System	6
Figure 4: LabVIEW GUI Screenshot for Running Demonstration	7
Figure 5: Maximum Theoretical Realized Q for Increasing Capacitance and Filter Order	9
Figure 6: Comparison of 2 nd -, 4 th -, 6 th -, and 8 th -Order Normalized Biquad Filter Responses for Various Q Values: Q=5 (Top Left), Q=10 (Top Right), Q=15 (Bottom Left) and Q=20 (Bottom Right)	10
Figure 7: Schematic of Ideal Biquad using Modeled Transconductors	16
Figure 8: Swept Bias Current for Control of Filter Center Frequency	16
Figure 9: Swept Bias Current for Control of Filter Q	17
Figure 10: Schematic of Ideal Biquad with Modeled Output Resistance	18
Figure 11: Filter Response with Decreasing Output Impedance	19
Figure 12: Schematic of Folded Cascode OTA	23
Figure 13: OTA Closed-Loop Gain for 1nA Bias	24
Figure 14: OTA Closed-Loop Gain for 100nA Bias	24
Figure 15: OTA Open-Loop Gain and Phase for 1nA Bias	25
Figure 16: OTA Open-Loop Gain and Phase for 100nA Bias	25
Figure 17: Biquad Filter Topology and Transfer Function	28
Figure 18: G_{m1} and G_{m2} Current Bias Sweep Controlling Filter Center Frequency	29
Figure 19: Center Frequency Vs. Bias Current Relationship Trendlin.....	29
Figure 20: G_{m3} Current Bias Sweep Controlling Filter Q	30
Figure 21: Quality Factor Vs. Bias Current Relationship Trendline	30
Figure 22: G_{m4} Current Bias Sweep Controlling Filter Gain	31
Figure 23: Gain Vs. Bias Current Relationship Trendline.....	31
Figure 24: G_{m3} Bias Current Sweep Controlling Q and Phase Margin	32
Figure 25: Minch Schematic	33
Figure 26: Minch I-V Curve for Bias Currents of 1nA, 10nA, 100nA, and 1uA	34
Figure 27: Minch Current Gain Sweep.....	34
Figure 28: Op-Amp Schematic.....	35
Figure 29: Op-Amp Closed-Loop Gain.....	36
Figure 30: OTA Open-Loop Gain and Phase.....	36
Figure 31: Schematic of Four Cascaded Biquad Filter Cells.....	37
Figure 32: Plot of Biquad Filter Bank with 2 nd -, 4 th -, 6 th -, and 8 th -Order Responses	38
Figure 33: Layout of MISA2 Chip	40

Figure 34: Monte Carlo Results of the Minch Current Mirror Mismatch Vs. Device Channel Length	41
Figure 35: MISA2 Fabricated Chip.....	43
Figure 36: MISA2 Test Board	45
Figure 37: DAC and Regulated Cascode Biasing Scheme	46
Figure 38: 2 nd -Order 10kHz Biquad Filter for Q=5,10, & 20	48
Figure 39: 8 th -Order 10kHz Biquad Filter for Q=5,10, & 20	48
Figure 40: Comparison of the Measured 2 nd -, 4 th -, 6 th -, 8 th -Order Biquad Filters and the MISA1 16 th -Order Filter.....	49
Figure 41: Normal (Left) and Zoomed (Right) Views of the 8 th -Order Biquad Filter and the MISA1 16 th -Order Filter Measured Frequency Response	49
Figure 42: 2 nd -Order 1kHz Biquad Filter with Varying Q=5,10,& 20.....	51
Figure 43: 8 th -Order 1kHz Biquad Filter with Varying Q=5,10,& 20.....	51
Figure 44: Gain Normalized 2 nd -Order 100kHz Biquad Filter with Varying Q=5,10,& 20	52
Figure 45: Gain Normalized 8 th -Order 100kHz Biquad Filter with Varying Q=5,10,& 20	52
Figure 46: 2 nd -Order 500kHz Biquad Filter with Varying Q=5,10,& 20.....	53
Figure 47: MISA2 Measured THD Spectrum of Both 2 nd - and 8 th -Order Filters ..	56
Figure 48: THD Comparison between 2 nd - and 8 th -Order Response for Increasing Input Amplitude.....	56
Figure 49: MISA2 Linear Dynamic Range for Low Q=5	58
Figure 50: MISA2 Linear Dynamic Range for High Q=20	58
Figure 51: Shared Bias Channel Biquads with Q=5 Demonstrates Mismatch Effects on Cascaded 2 nd -Order Filters.....	61
Figure 52: Zoomed 2 nd -Order 1kHz MISA2 Biquad Filter of Three Chips	62
Figure 53: Zoomed 8 th -Order 1kHz MISA2 Biquad Filter of Three Chips	63
Figure 54: Zoomed 2 nd -Order 10kHz MISA2 Biquad Filter of Three Chips	63
Figure 55: Zoomed 8 th -Order 10kHz MISA2 Biquad Filter of Three Chips	64
Figure 56: Zoomed 2 nd -Order 100kHz MISA2 Biquad Filter of Three Chips	64
Figure 57: Zoomed 8 th -Order 100kHz MISA2 Biquad Filter of Three Chips	65
Figure 58: Frequency-Controlled Current Bias for Q=10 of Three Chips	66
Figure 59: Frequency-Controlled Current Bias for Q=10 of Four Individual Biquads on Chip2	67
Figure 60: Q-Controlled Current Bias for Q=10 of Three Chips	67
Figure 61: Q-Controlled Current Bias for Q=10 of Four Individual Biquads on Chip2	68
Figure 62: Gain-Controlled Current Bias for Q=10 of Three Chips	68
Figure 63: Gain-Controlled Current Bias for Q=10 of Four Individual Biquads on Chip2	69

CHAPTER ONE

INTRODUCTION

Motivation

Remote sensing networks is an evolving technology that has enabled the realization of the Internet of Things (IoT), commonly defined as a network of embedded, internet connected physical devices that interact and collect and exchange data. There are numerous applications for the IoT across all technology sectors including commercial, industrial, and government. Use in industrial applications, such as the Smart Grid and power generation, may include platform specialization to facilitate both system health monitoring and predictive maintenance. Associated common methods include motor current and vibrational analysis with an emphasis on identifying particular signal frequency components. This work focuses on realizing a key hardware component for many of these monitoring and/or control hardware platforms – a very low power, programmable analog filter that will enable highly efficient signal signature analysis.

Objective

One of the challenges for a remote sensing platform is obtaining a balance between very low power operation (enabling a long dwell time battery operated sensor) and high-fidelity data processing (typically requiring large amounts of power) for optimized signal detection. Digital Signal Processing (DSP) excels at high performance data processing but can require excessive amounts of power, a requirement not suitable for battery-powered remote sensing applications. Thus, the primary objective of this research is to realize an Analog Signal Processing

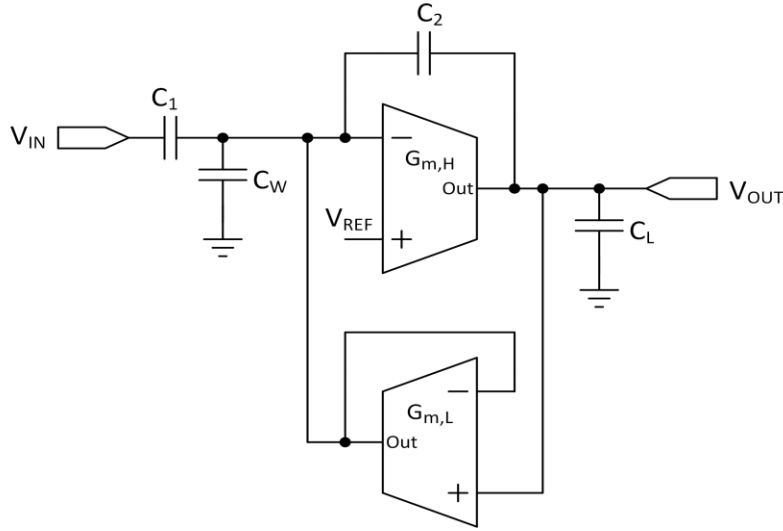
(ASP) front-end that when coupled with a low-power microcontroller backend, could provide sufficient performance to meet our platform goals: very low power operation for extended dwell times, and sufficient sensitivity for limited signal spectral analysis. For vibrational analysis, the ASP-based solution will need to perform harmonic discrimination at multiple target frequencies. The ASP-based programmable filter developed in this work will enable platforms capable of performing very lower power, digitally controlled spectrum scanning and discrimination.

CHAPTER TWO

BACKGROUND

Previous Work

The work presented in this thesis builds on the preceding research for a similar project conducted by Ben Roehrs [1]. The purpose of this thesis is to leverage the successes of the previous work, while improving the performance and efficiency using a unique filter design. The prior research presented a Multi-channel Integrated Spectrum Analyzer (MISA1) which utilized a monolithic, high-order filter system with off-chip biasing and signal buffer circuits. The integrated circuit consisted of two filter channels. Each channel was comprised of four cascaded OTA-C4 [1] (Operational Transconductance Amplifier – Four Capacitors) filters shown in Figure 1, with intermediate output buffers and Minch current mirror biasing (not shown). Each OTA-C4 cell was designed to have a fixed quality factor of ~ 2.1 .



$$\frac{V_{out}}{V_{in}} = -\frac{C_1}{C_2} \frac{s\tau_l(1 - s\tau_f)}{1 + s(\tau_l + \tau_f(\frac{C_2}{C_1} - 1)) + s^2\tau_h\tau_l}$$

Figure 1: Schematic and Transfer Function of the 2nd-Order OTA-C4 Filter (MISA1)

Results

The MISA1 chip can scan a spectral band of 2kHz [kilohertz] to >100kHz with an ‘effective’ quality factor (Q) of 6, if configured as a 16th-order filter (eight 2nd-order C4-OTA cells in series). The measured transfer function for this MISA1 filter configuration is plotted in Figure 2 for six different center frequencies. A test system was developed and built to demonstrate the functionality of the chip with PC-based programmability of the filter functions for automated spectral analysis (see Figure 3). This was completed using a custom printed circuit board (PCB) incorporating an SPI (Serial Peripheral Interface) port for programming the DACs (Digital-to-Analog Convertors), enabling digital control of the MISA1 filter center frequency via bias current programming. A MISA1 control and spectral analysis program displayed in Figure 4 was created using LabVIEW and an Agilent multi-function data acquisition module (Agilent U2531A, 4 Channel, Simultaneous

Sampling, 14 Bits, 2MS/s) used to provide both digital control and signal digitization. With the system complete, a full demonstration was conducted using representative sensor signals and the analysis results indicated successful classification of a signature of harmonic signals. The MISA1 tests demonstrated the feasibility for very low power detection of the target signals and supported the premise for a highly miniaturized, very low power signal signature analysis system based on the MISA1 chip.

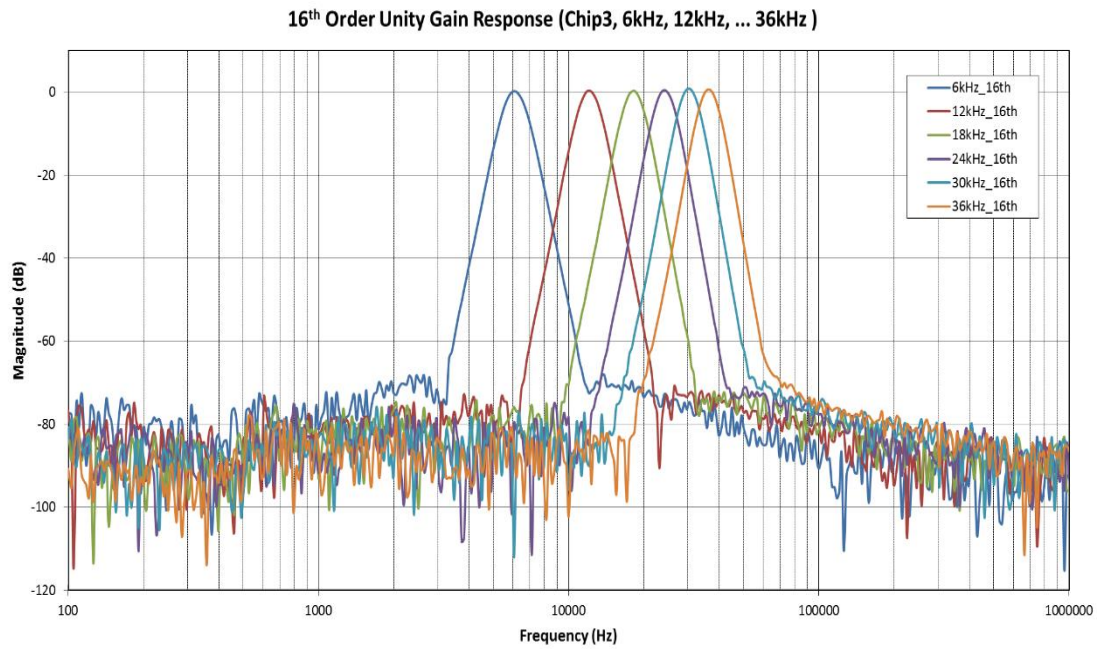


Figure 2: MISA1 16th-Order Response at 6kHz and Multiple Harmonic Frequencies

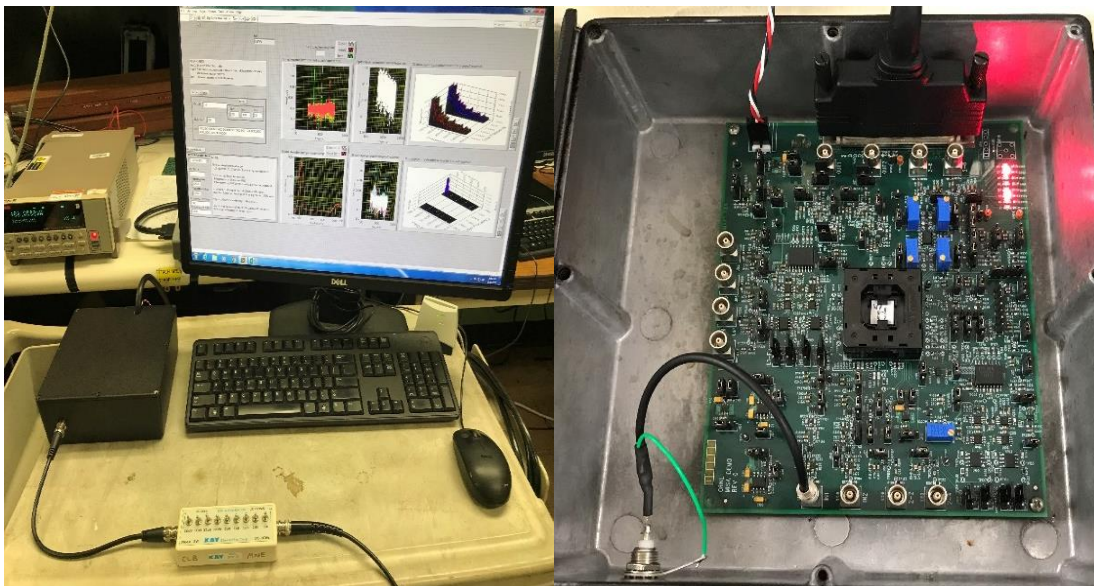


Figure 3: MISA1 Demonstration System

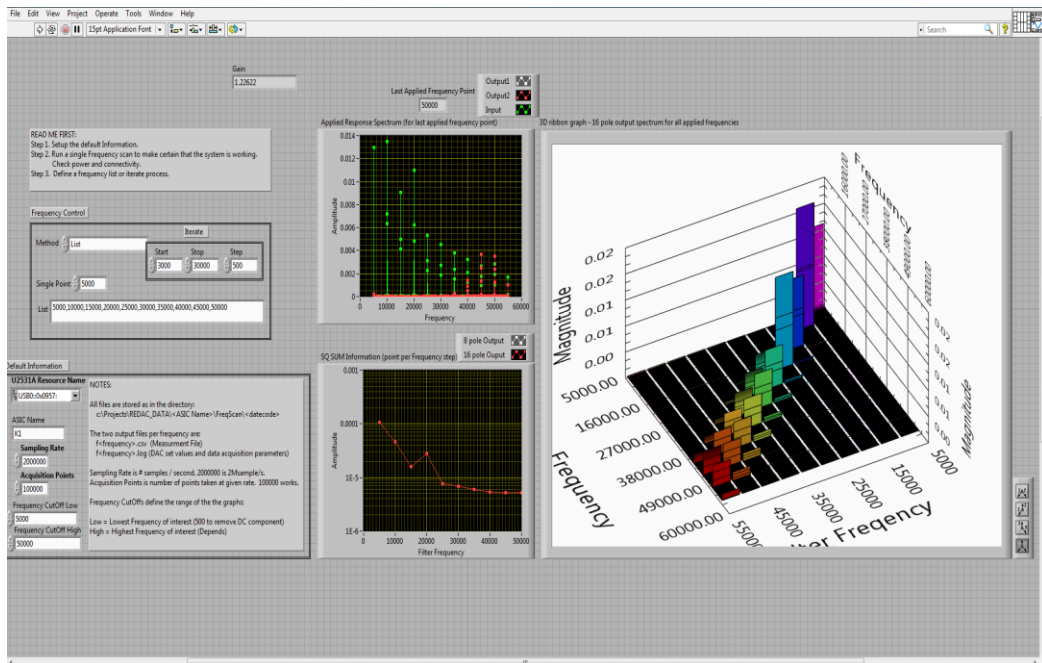
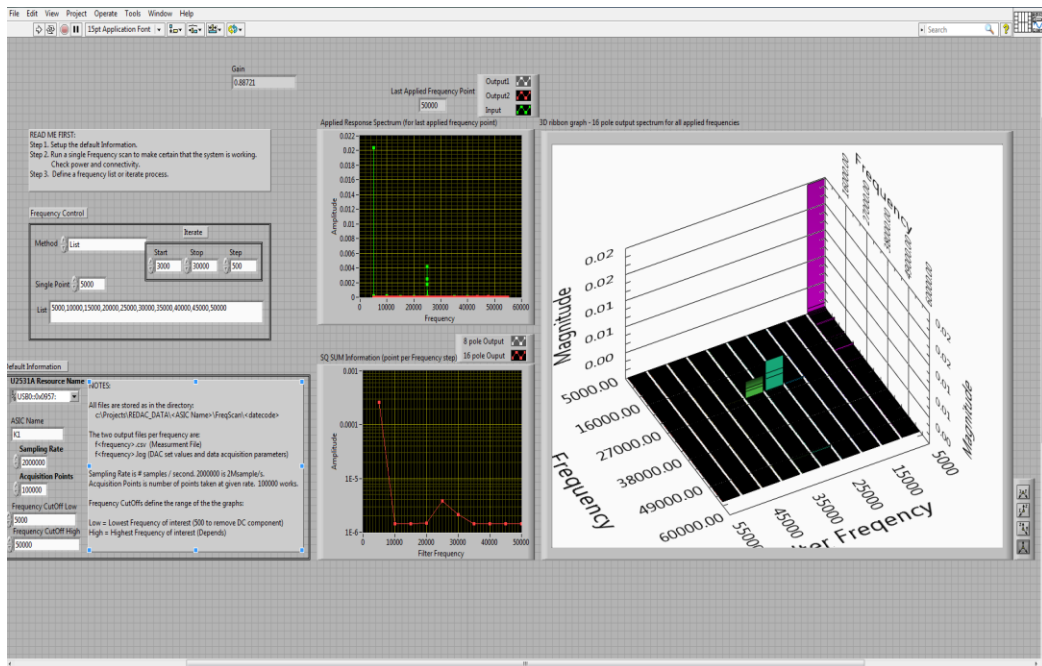


Figure 4: LabVIEW GUI Screenshot for Running Demonstration

Improvements

While the original MISA1 chip performed well, further improvements in system operation through increased spectral selectivity are possible by increasing the quality factor (Q) of the filter transfer function. Methods for improving the overall filter Q were investigated beginning with a re-evaluation of the MISA filter topology for maximizing Q. However, the MISA1 topology would require use of a very large integrated capacitance and a very well matched high-order filter cascade to accomplish this, as demonstrated in Figure 5 for the ideal circuit. The use of a super heterodyne mixer and low-pass filter architecture was also investigated since it is common in higher end spectrum analyzers. However, the requirement for a tunable, low distortion reference signal and its associated power consumption made this topology undesirable. In addition, other filter designs having much increased Q were simulated in SPICE including topologies based on gyrator-C active filters and biquadratic active filters with variable Q adjustment. This investigation (see Figure 6) shows the theoretical range of filter performance possible. Each plot illustrates the filter response for increasing filter order for a fixed quality factor. From the top left plot to the bottom right plot the fixed Q is increased to demonstrate the response differences from the filter order. These plots are continually compared to the MISA1 measurements of the 16th-order response to justify the needed improvements for the filter design.

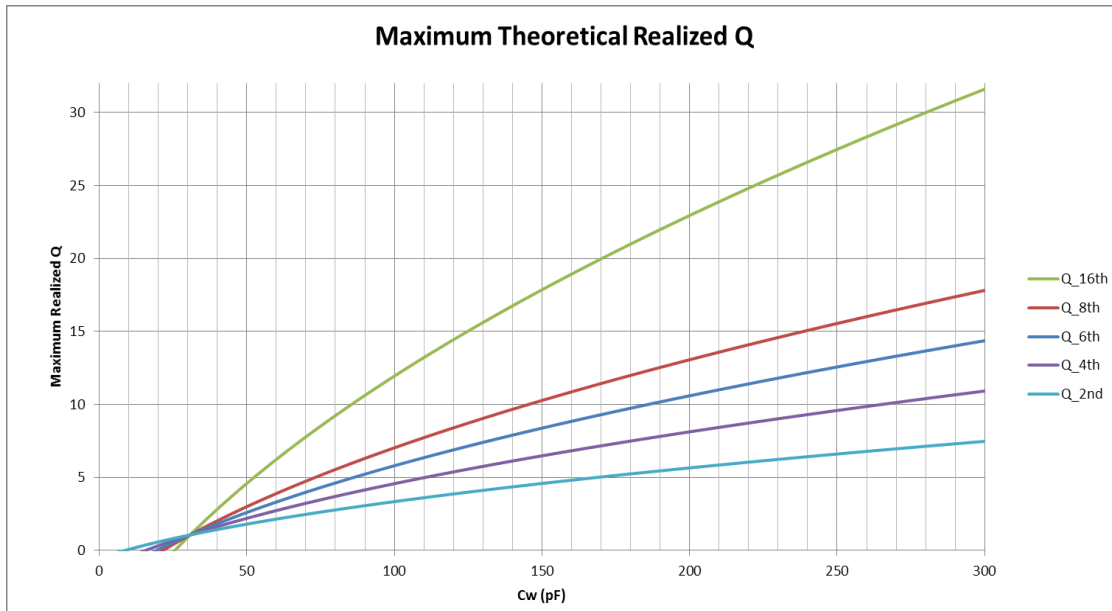


Figure 5: Maximum Theoretical Realized Q for Increasing Capacitance and Filter Order

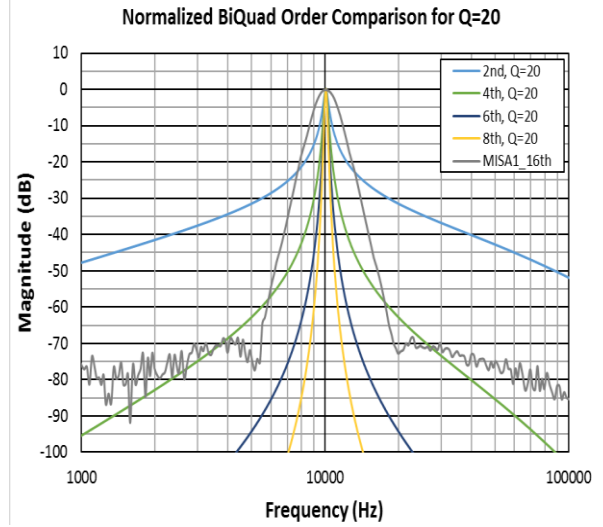
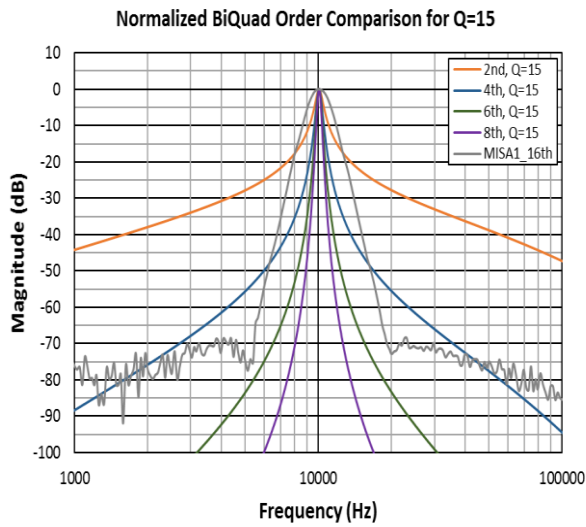
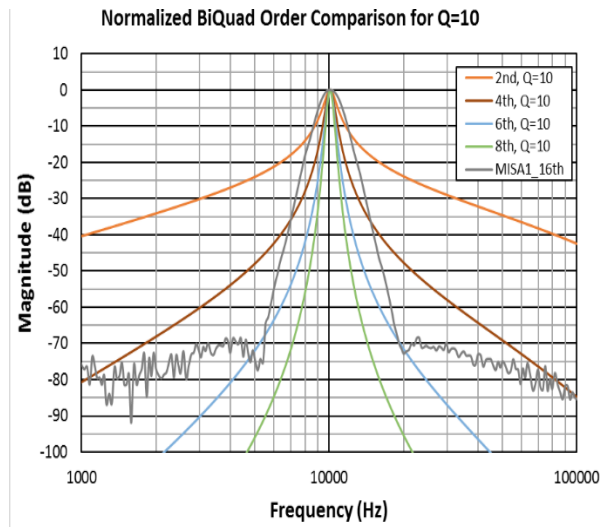
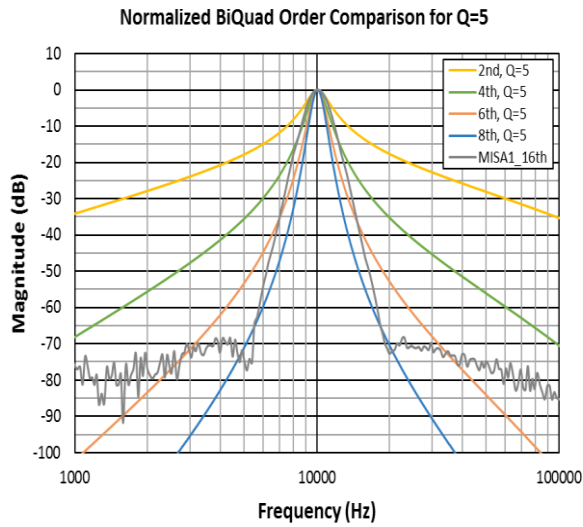


Figure 6: Comparison of 2nd-, 4th-, 6th-, and 8th-Order Normalized BiQuad Filter Responses for Various Q Values: Q=5 (Top Left), Q=10 (Top Right), Q=15 (Bottom Left) and Q=20 (Bottom Right)

Literature Review

Initially, a wide array of books and publications were studied for background information on analog filter design. This was carried out to refresh the basics of circuit analysis for complex transfer functions, to develop a sense of practical design from common techniques demonstrated in literature, and to review the diversity of solutions available to direct efforts towards more promising filter architectures. Thus, multiple techniques for highly selective filter were evaluated including the following: analog active filter banks, active inductor or gyrator-C topologies, biquadratic active filters, and Gm-C filters. Eventually, the final design would implement several features of these different techniques in order to utilize the advantages offered by each for constructing a robust filter design.

References on Filters

The Gm-C filter [2] can be the basis for many of these techniques, although it is not always required. This topology consists of at least one transconductor and one capacitor. In its simplest form a series combination produces a low-pass filter, while a parallel combination produces a high-pass filter. What stands out is the transconductor, which can be tuned to a specific value using a bias current, as often utilized in an OTA (operational transconductance amplifier). These Gm-C filters are the building blocks for various filter responses and are implemented readily from a desired transfer function. The simple derivation of a Gm-C filter is also very appealing, because a desired transfer function can be used to rapidly generate a filter topology.

The primary reference for the MISA1 filter was a low-power high-order analog filter bank presented by Graham et al. in [3] and [4]. This technique took advantage of cascaded filters to achieve a higher performance filter with minimal power consumption of each cell. While it also included floating gate transistors for a low-power bias network, this was not implemented in our previous work due the

complexity of programming floating gates. However, this approach is limited in the spectral selectivity that is practically obtainable, since very large capacitors and/or very high filter order would be necessary to achieve the desired response for our application.

The active inductor, also known as the gyrator-C, is a filter topology that can produce very high spectral selectivity using minimal stages, with a reasonable capacitance spread. Using this architecture Sundarasrandula et al. [6] demonstrated a 1-V, 6nW programmable 4th-order filter that achieved a quality factor, Q , of up to 50. This technique was also implemented by Duan et al. [7] for a high Q band-pass filter at 46MHz. However, this topology is susceptible to stability issues as any high Q circuits would also encounter. Thus, this type of design must consider precision and matching of circuit components to ensure stability during operation.

Biquadratic filters offer a flexible architecture with independent control over filter characteristics. A biquadratic topology can be generated from a desired transfer function, which allows simple modifications to a circuit topology without complex derivations for the new transfer functions. One example of this architecture is given by Geiger et al. [5]. With the ability to tune circuit components independently, the filter characteristics can be swept, remain constant, or act as a function of another characteristic. For instance, the Q of a biquadratic filter can be set to linearly increase with the center frequency. These advantages of the biquadratic transfer function make it an appealing approach for tunable filter designs.

CHAPTER THREE

DESIGN DEVELOPMENT

Specifications and Requirements

In order to begin the formal design process, a set of specifications and requirements were necessary to narrow the design choices. The primary specifications include the following: programming of the filter center frequency from 1kHz-100kHz, programming of the filter selectivity (or Q) with the minimum Q of 10, programming of the filter cell gain ($\pm 3\text{dB}$) to maintain an overall filter channel gain of approximately 0dB, and minimal power consumption at or below the 155 μW measured for MISA1, while maintaining the above specifications. Secondary requirements included the following: maximized linear dynamic range to maximize the filter SNR with a fixed noise floor, the ability to cascade the 2nd order filter sections to obtain higher order filter responses, and the ability to observe each filter output signal.

Filter Characteristics

With the general specifications of the filter channel determined, the characteristics of the band-pass filter cell could be derived. The ideal 2nd-order transfer function, shown in Equation 1, could be examined for the primary components that established the filter response. The center frequency, f_o , of the band-pass response is determined by the term $\omega_o = \frac{f_o}{2\pi}$, and will be determined by the two poles and the zero. The 3dB bandwidth of the filter, $\frac{\omega_o}{Q}$, sets the 3dB-width of the passband of the band-pass filter. The center frequency divided by the 3dB bandwidth gives the quality factor, Q, of the filter which is a unit-less term that can be compared across the spectrum. Finally, the gain of the filter, H_o , is the output-

to-input signal gain at the peak of the passband function. These characteristics can be equated to the requirements for the frequency range, 1kHz-100kHz, and the quality factor, greater than or equal to 10.

$$H(s) = \frac{H_o \frac{\omega_o}{Q} s}{s^2 + \frac{\omega_o}{Q} s + \omega_o^2} \quad Eq. (1)$$

Design Methodology

System Architecture

Candidate system architectures were explored and compared in terms of the functional advantages, disadvantages, and practicality of implementation. A filter bank architecture has proven beneficial for increasing performance of a single 2nd-order filter cell, but without significant improvement over the MISA1 design would require too many resources to obtain the desired spectral selectivity. Consequently, significant improvement in the narrowband characteristics of the base 2nd-order filter cell (higher Q) was targeted, which would enable much improved spectral selectivity, using significantly fewer cascaded stages than required using the MISA1 design. The combination of Gm-C high-pass and low-pass filters has proven to obtain a limited quality factor. The active inductor or gyrator-C circuit can acquire a very narrowband response for a 2nd-order system but can lead to an unstable filter if not properly implemented. So, a method enabling fine control of the Q, and therefore the stability of filter, was determined essential. From the previous filter topology review, Gm-C based filters provide the ability for fine Q control. Gm-C cells can easily be configured to implement a wide range of transfer functions, but also allow a specific circuit component to be modified with the bias current of the transconductor. Thus, the Gm-C network was

selected for implementing desired filter characteristics, including control of the filter center frequency and quality factor.

Behavioral Modeling for High-Level Design

In order to confirm the functionality of this system architecture, behavioral models were simulated using LTspice. Both ideal transconductors and capacitors were used to verify the ideal performance of this topology, as shown in the schematic of Figure 7. The ideal waveforms in Figure 8 confirm the desired transfer function swept across the target spectrum. This topology also has the added benefit of a unity gain peak response which is ideal for the application. Transconductances G_1 and G_2 are biased for a specific frequency, and also form the active inductor when combined with the capacitor C_1 . Therefore, the active inductor and the parallel capacitor, C_2 , form a resonant LC tank circuit. This resonance is determined by the ratio of the two capacitors, which may be too small for the application or too large resulting in oscillation. To mitigate these G_3 acts as an active resistor that has damping effect on the circuit that prevent instability and allows a variable selectivity as shown in Figure 9.

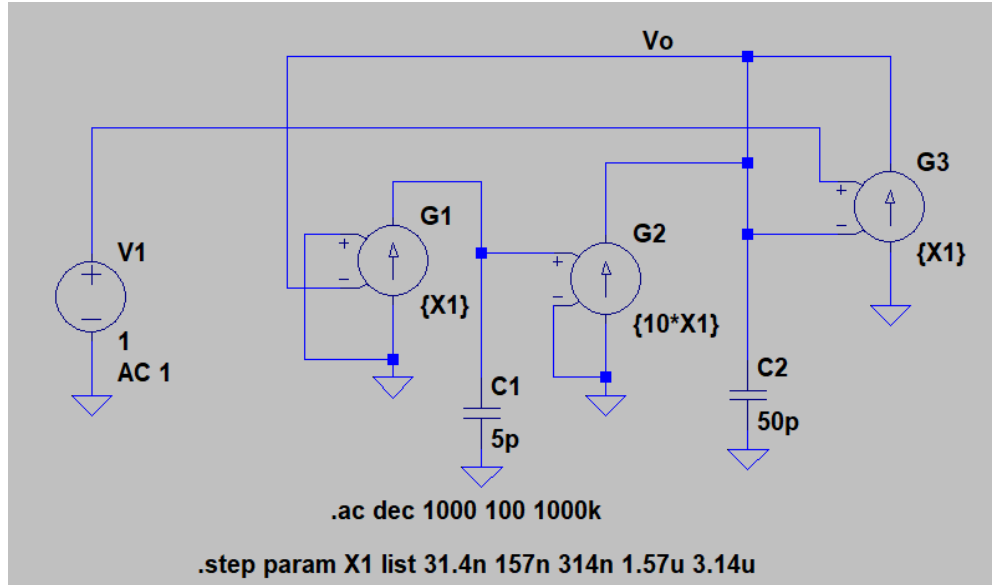


Figure 7: Schematic of Ideal Biquad using Modeled Transconductors

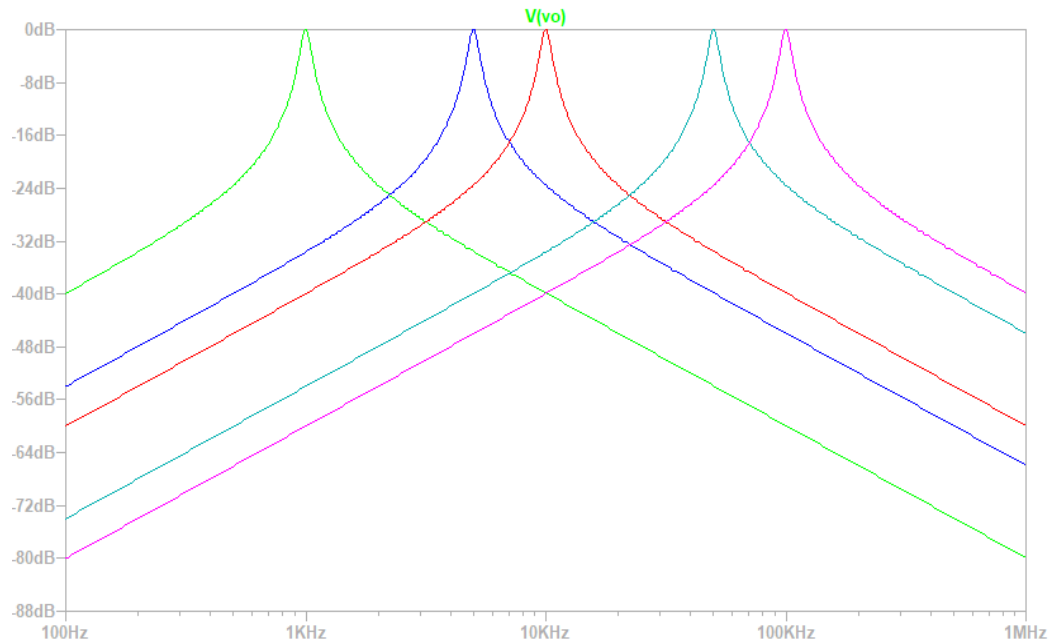


Figure 8: Swept Bias Current for Control of Filter Center Frequency

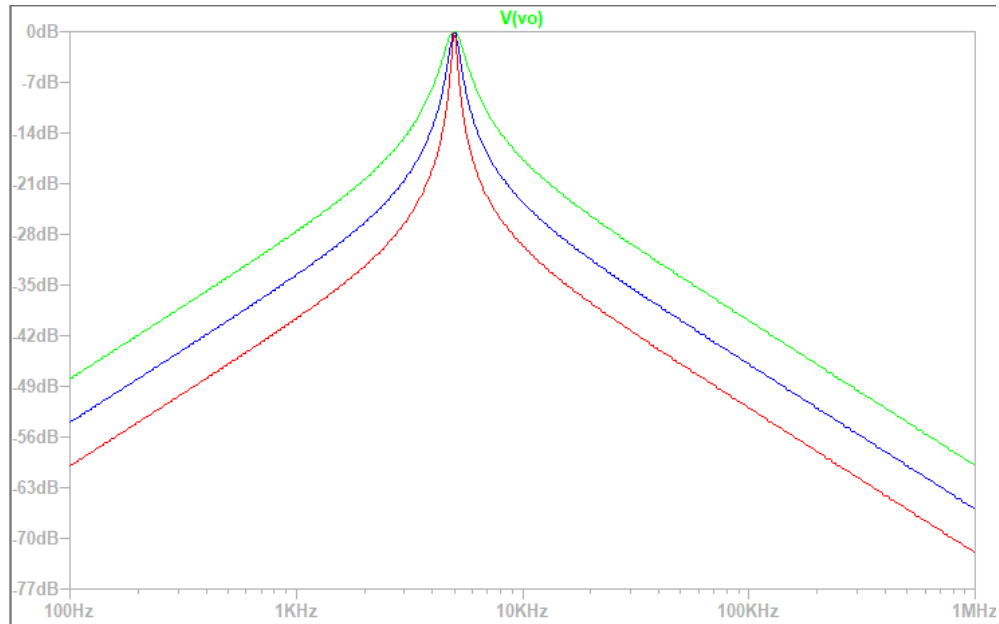


Figure 9: Swept Bias Current for Control of Filter Q

Unfortunately, the ideal simulations did not reveal a flaw in this architecture that was discovered when simulating with real integrated process models. This non-ideality was verified using LTspice and was determined to result from the finite output resistance of each transconductor. In the ideal model, the output of each transconductor sees only the capacitance load in parallel with an infinite resistance, so the output current will allow charging of the capacitor creating the ideal time constant of the Gm-C circuit. With finite output resistance the transconductor current will split proportionally between the load capacitor and non-infinite resistor as shown in the schematic in Figure 10. The resulting effect on the transfer function is normally negligible, but if this output resistance becomes too small then a resultant low-frequency zero will approach the filter response. This becomes apparent within a few decades of the center frequency but can also have

a detrimental effect on the filter response if the output resistance becomes comparable to transconductors as shown in Figure 11. This non-ideality will be considered in the low-level design of the transconductors themselves. This effect also contributes to non-ideal gain of the transfer function, which requires an extra transconductor to maintain a unity gain response.

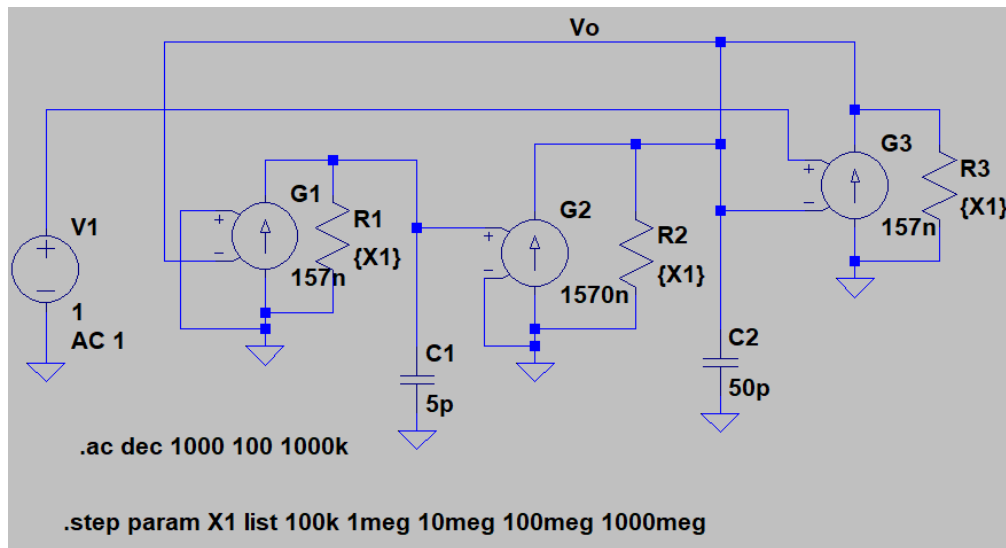


Figure 10: Schematic of Ideal Biquad with Modeled Output Resistance

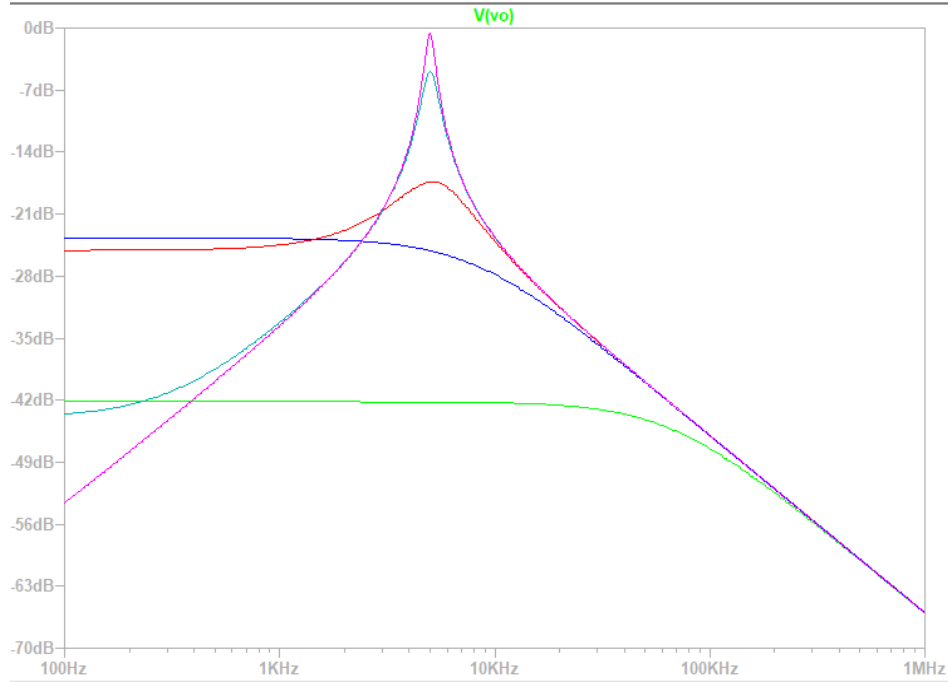


Figure 11: Filter Response with Decreasing Output Impedance

Circuit Topologies

The behavioral performance of the general filter transfer function was verified using simplified circuit blocks and models, as shown in the previous section. In this section, the transfer functions will be implemented as practical circuits and verified using detailed integrated circuit process simulation models.

The base filter cell is the most important circuit block in this design, as it drives the overall function of the low-power programmable filter channel. Based on the previous behavioral model simulations for the Gm-C block, this topology was originally chosen and implemented but modified with a fourth transconductor that allowed for control of gain. This topology was nicknamed the biquad filter since the transfer function resembled the biquadratic response. The biquadratic transfer function (see Equation 2) contains a polynomial in the numerator and denominator. The numerator consists of terms related to different inputs to filter circuit that create

a high-pass, band-pass and low-pass functions: $V_{HP}s^2 + V_{BP}s + V_{LP}$. In this case, the high-pass and low-pass inputs are grounded and reduce to the equation to the generic band-pass function as seen in Equation 1.

$$H(s) = \frac{V_{HP}s^2 + V_{BP}s + V_{LP}}{s^2 + \frac{\omega_o}{Q}s + \omega_o^2} \quad Eq. (2)$$

As discussed in the previous section this topology required robust transconductors to mitigate the effect of finite output impedance. Each transconductor would also need to be variable to control each of the filter's characteristics. Therefore, an operational transconductance amplifier (OTA) was chosen with a current biased differential pair and a folded cascode output stage for much higher output impedance. The linearity of these transconductors was a major concern since this would limit the input signal size allowed to maintain linearity and small-signal assumptions. A bump differential pair was added for a boost to the OTA linearity.

Along with the main biquad filter cell, two other circuits were needed: the buffer located between cascaded filter cells, and the biasing scheme for the variable OTA's. The buffers were chosen to be robust operational amplifiers (Op-Amps) in unity gain configuration using negative feedback. The Op-Amp topology was designed as a current biased differential pair with Class AB output stage and added compensation for adequate bandwidth and stability. The biasing scheme, based on the circuit introduced by Minch [8], was designed as a high input and output resistance current mirror that maintains saturation throughout a very wide current range. Using these components, a filter bank channel will be constructed composed of four biquad filter cells, an Op-Amp buffering between stage, and at least five Minch current mirrors composed of the bias currents for the biquad filter cell and Op-Amp buffer. In the final filter channel implementation, the current

mirrors will be digitally programmed off-chip for control of each filter cell's gain, quality factor, and center frequency.

Technology Current Extraction

The sizing of the transistors used in the OTA depends on three major points. First, the required frequencies and capacitors implemented determine the necessary transconductance for each filter's characteristics. Second, the inversion coefficient for each device sets the relationship between bias current and transconductance. In the subthreshold region, or weak inversion, transconductance is related linearly with bias current and is also the most power-efficient mode of operation. Third, the length of each will be optimized using longer channel lengths for best matching against short-channel effects and process variation; while also reducing channel length for parasitic capacitance that reduce bandwidth.

$$\text{Inversion Coefficient } [IC] = \frac{I_D}{2n\mu C'_{ox} U_T^2 \frac{W}{L}} = \frac{I_D}{I_0 \frac{W}{L}} \quad \text{Eq. (3)}$$

$$\text{Weak Inversion: } IC \leq 0.1$$

$$\text{Moderate Inversion: } 0.1 < IC < 10$$

$$\text{Strong Inversion: } IC \geq 10$$

The inversion coefficient describes the three biasing schemes of a saturated transistor. Equation 3 shows the expression for the inversion coefficient and lists the three different types of inversion modes: weak, moderate, and strong as derived from Binkley [9]. Weak inversion is where the channel is barely inverted, the gate-source voltage is below the threshold voltage of the device, and the transconductance is linear with current. This regime generally has the lowest values of transconductance and high power efficiency. Strong inversion where the channel is fully inverted, the gate-source voltage is well above the threshold

voltage of the device, the transconductance is a square root function of current, and generally has the highest values of transconductance with poor power efficiency. Moderate inversion is the transitional period between them and is not simply described with a single equation but produces a balance of transconductance and power efficiency. The transistors were designed to operate in the weak inversion region throughout the frequency range. Therefore, the devices were sized so that they would remain in weak inversion above 100kHz with some margin for error. This was verified with a sized transistor and current sweep simulation.

Simulation

Simulation of the chosen circuit topologies were conducted using Cadence's Virtuoso Analog Design Environment (ADE). All simulations were performed using foundry provided process development kit (PDK) device models. Note that the following simulation plots represent models from any generic standard 1.8V core, 180nm process and do not represent any specific integrated circuit fabrication process or foundry.

Operational Transconductance Amplifier

The topology implemented for the OTA is a current biased differential pair with a bump degeneration and a folded cascode output stage. Figure 12 shows the Cadence schematic for the OTA cell. The input bias current is mirrored with a PMOS cascode to an output biasing branch and the source of the PMOS differential input pair. The four transistor bump degeneration acts as cross-coupled, source degeneration resistors. The output of the differential pair is fed to the high impedance folded cascode output stage.

Simulations verified the expected performance of the OTA. Figure 13 shows a Bode plot of the closed loop gain with a bias current of 1nA and a 1pF load, while

Figure 14 is a for a bias current of 100nA, for higher frequency operation. The gain is unity until the cutoff frequency is reached at $\sim 15\text{kHz}$. Figure 15 is a Bode plot of the open loop gain and phase with a bias current of 1nA and a 1pF load, while Figure 16 is for a high frequency bias of 100nA. The open loop testbench also includes an infinite feedback resistor and infinite shunting capacitor to act as an AC open circuit and a DC short circuit. The open loop gain is measured as $\sim 85\text{dB}$ with a crossover frequency of $\sim 12\text{kHz}$. The phase at the crossover frequency is measured as 85° .

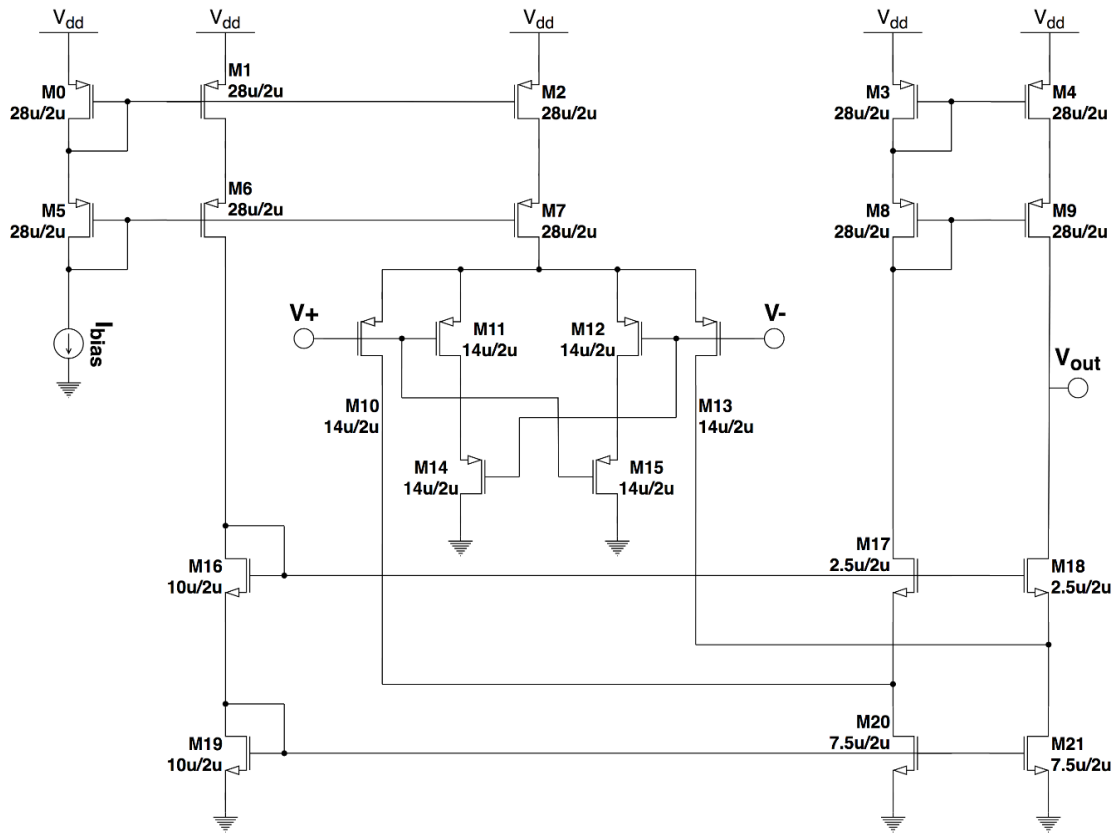


Figure 12: Schematic of Folded Cascode OTA

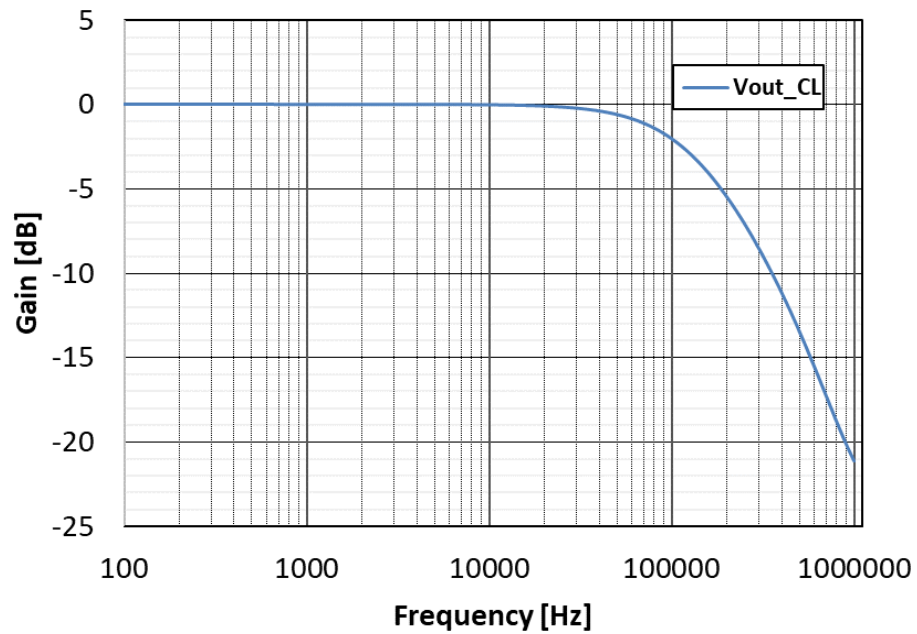


Figure 13: OTA Closed-Loop Gain for 1nA Bias

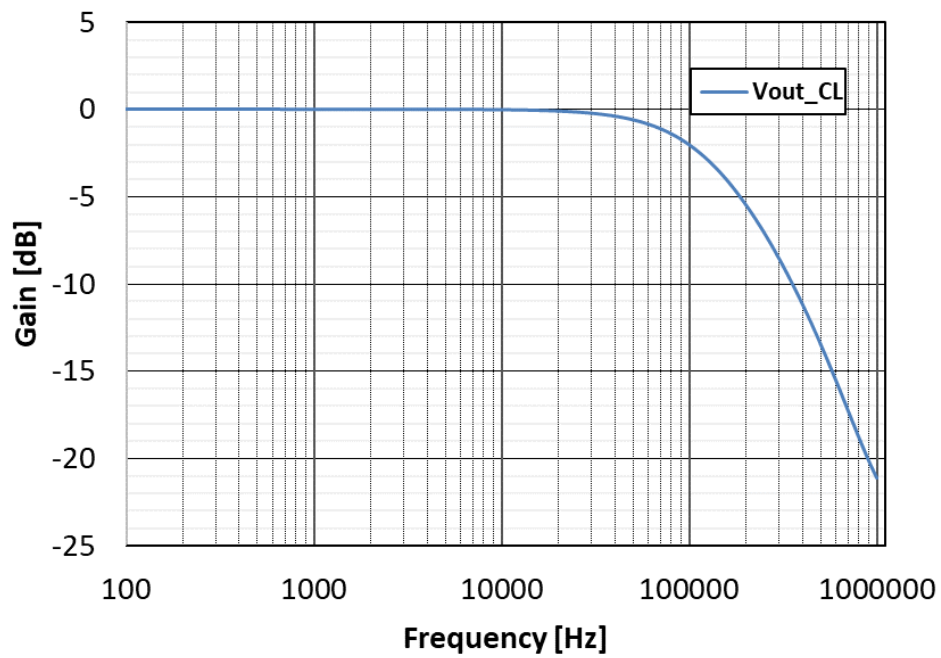


Figure 14: OTA Closed-Loop Gain for 100nA Bias

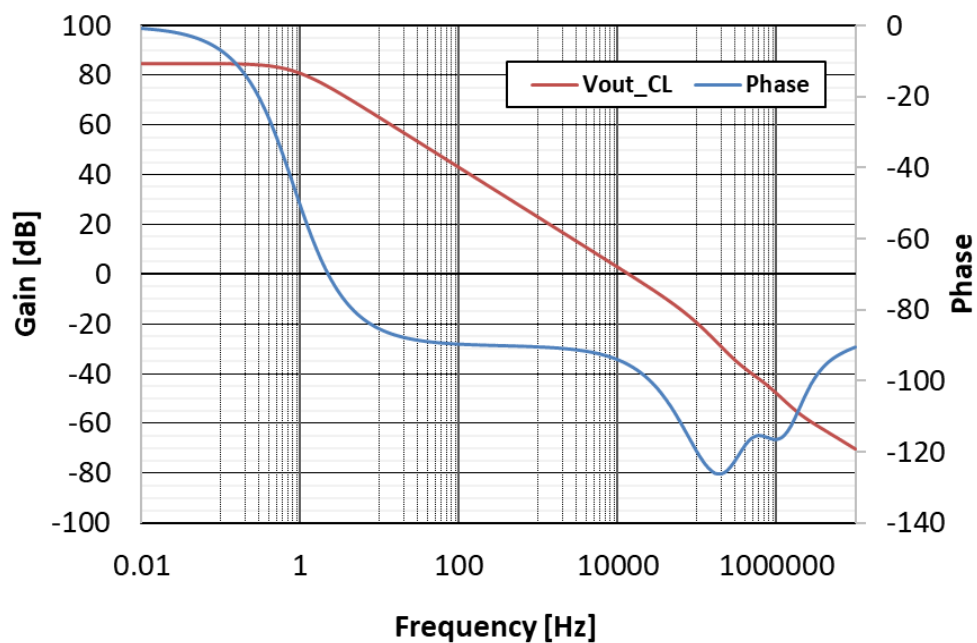


Figure 15: OTA Open-Loop Gain and Phase for 1nA Bias

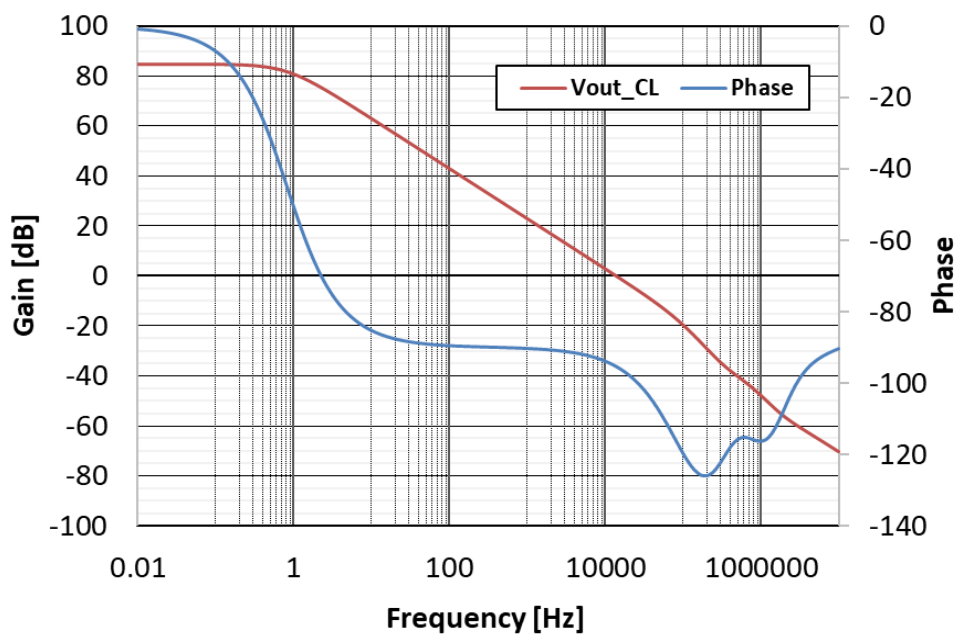


Figure 16: OTA Open-Loop Gain and Phase for 100nA Bias

Biquad Filter Cell Optimization

The biquad filter cell was designed as a Gm-C based active inductor architecture with a biquadratic transfer function. Ideally, the filter acted as a resonant RLC filter, but had some non-idealities that were either mitigated with further design or were mainly present when operated beyond the initial intended range for higher frequencies. As shown in Figure 17 the schematic contains two capacitors and four OTA's. G_{m1} and G_{m2} , along with C_2 , represent the active inductor which sets the center frequency with C_1 . G_{m3} is an active resistor that dampens the resonance of the biquad filter. G_{m4} is attenuator that is used to compensate for the effects of non-idealities on the gain. The filter characteristics can be extracted by comparing the biquadratic transfer function to that of standard band-pass function. The angular frequency is defined in Equation 4. Using this the quality factor can be determined by dividing the angular frequency by the bandwidth as shown in Equation 5. Finally, the gain can be calculated using the numerator and quality factor in Equation 6.

$$\omega_o = \sqrt{\frac{G_{m1}G_{m2}}{C_1C_2}} \quad Eq (4)$$

$$Q = \omega_o \div \frac{\omega_o}{Q} = \frac{1}{G_{m3}} \sqrt{\frac{G_{m1}G_{m2}C_1}{C_2}} \quad Eq (5)$$

$$H_o = H_o \frac{\omega_o}{Q} \div \frac{\omega_o}{Q} = \frac{G_{m4}}{C_1} \div \frac{G_{m3}}{C_1} = \frac{G_{m4}}{G_{m3}} \quad Eq (6)$$

From here, the sensitivity of the filter can be analyzed to further understand the dependence of the filter characteristics on circuit components. The sensitivity of a dependent variable, y , with respect to an independent variable, x , is defined as shown in Equation 7. This essentially gives the proportional factor between these two factors. The sensitivity of the angular frequency is a factor of positive or negative one half for each variable as defined in Equation 8. This is similar for the quality factor, except that Q is dependent on G_{m3} by a factor of one as seen in

Equation 9. The gain sensitivity is dependent on either G_{m3} or G_{m4} by a factor of positive or negative one as derived in Equation 10. This completed sensitivity analysis expressed the variable dependencies for each filter characteristic, but also allowed us to consider the effect of component or process variation on the performance of the filter.

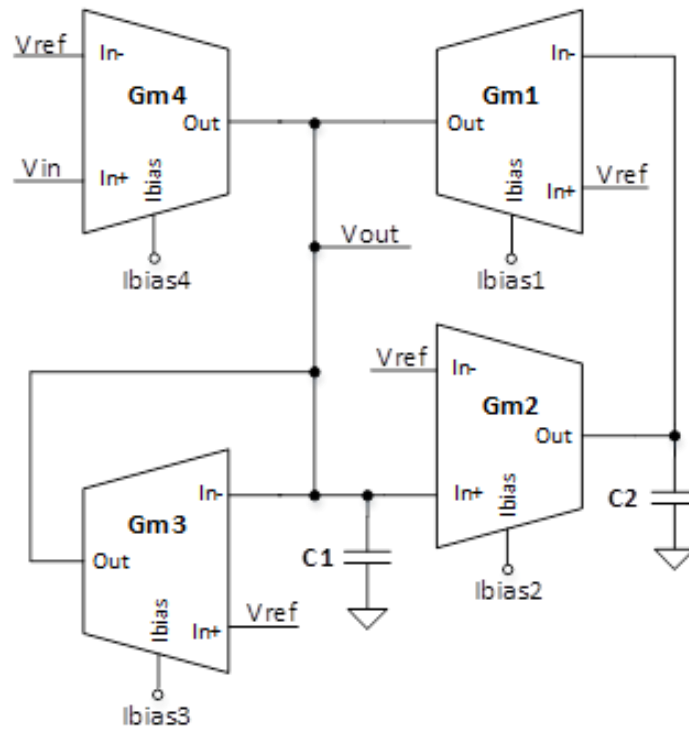
$$S_x^y = \frac{x}{y} * \frac{\partial y}{\partial x} \quad Eq. (7)$$

$$S_{G_{m1}}^{\omega_o} = S_{G_{m2}}^{\omega_o} = \frac{1}{2}; \quad S_{C_1}^{\omega_o} = S_{C_2}^{\omega_o} = -\frac{1}{2} \quad Eq. (8)$$

$$S_{G_{m1}}^Q = S_{G_{m2}}^Q = S_{C_1}^Q = \frac{1}{2}; \quad S_{C_2}^Q = -\frac{1}{2}; \quad S_{G_{m3}}^Q = 1 \quad Eq. (9)$$

$$S_{G_{m3}}^{H_o} = -1; \quad S_{G_{m4}}^{H_o} = 1 \quad Eq. (10)$$

With these filter characteristics extracted and well defined, the biquad filter cell can be optimized for the operation frequencies, quality factor, biasing scheme, sizing constraints. Ultimately, the OTA differential pair transistors were sized as $14\mu\text{m}$ and $2\mu\text{m}$ for gate width and length, respectively; while the capacitors, C_1 and C_2 , were sized as 20pF and 2pF, respectively. The capacitor ratio affects the quality factor of the filter as seen in Equation 3, by a square root factor. This optimized filter cell was simulated across the frequency range of 1kHz-100kHz (see Figure 18). The relationship trendline between frequency and bias current can be seen in Figure 19. The variable quality factor and its relationship to bias current are demonstrated in Figure 20 and Figure 21, respectively. The variable gain and its relationship to bias current are demonstrated in Figure 22 and Figure 23, respectively. The stability of the resonant filter was also a major consideration. Figure 24 demonstrates how both quality factor (blue) and phase margin (red) are inversely proportional and can be swept using the bias current for G_{m3} . This was important as it confirmed that the stability of the filter was tunable and also inversely proportional to the quality factor.



$$H(s) = \frac{s \frac{G_{m4}}{C_1}}{s^2 + s \frac{G_{m3}}{C_1} + \frac{G_{m1} G_{m2}}{C_1 C_2}}$$

Figure 17: Biquad Filter Topology and Transfer Function

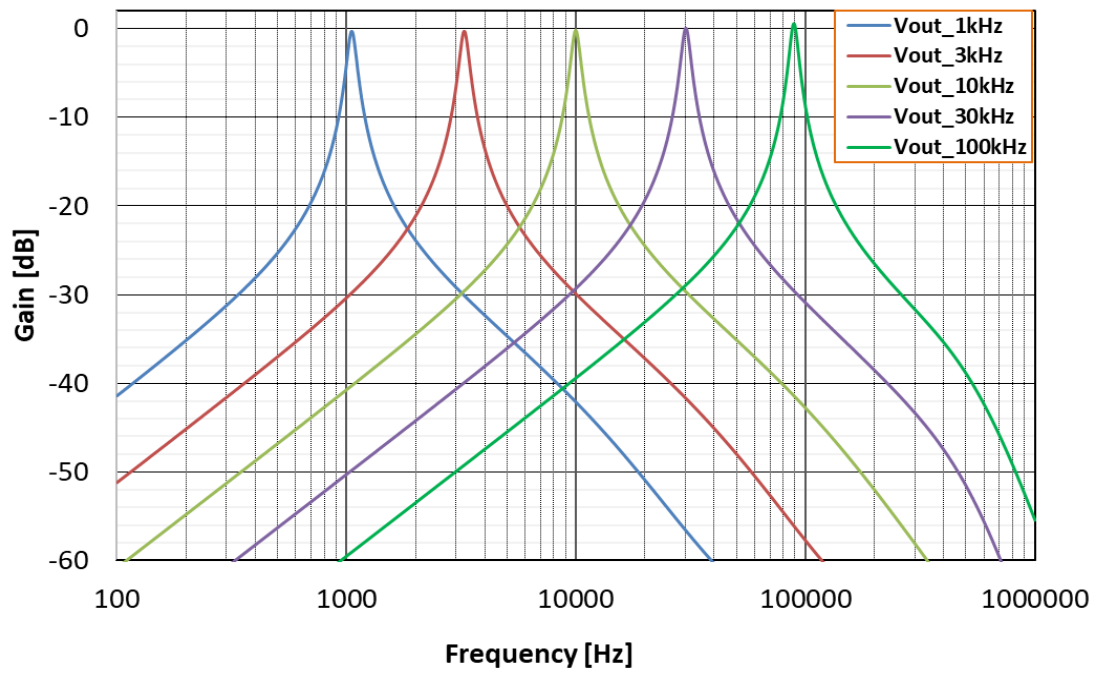


Figure 18: G_{m1} and G_{m2} Current Bias Sweep Controlling Filter Center Frequency

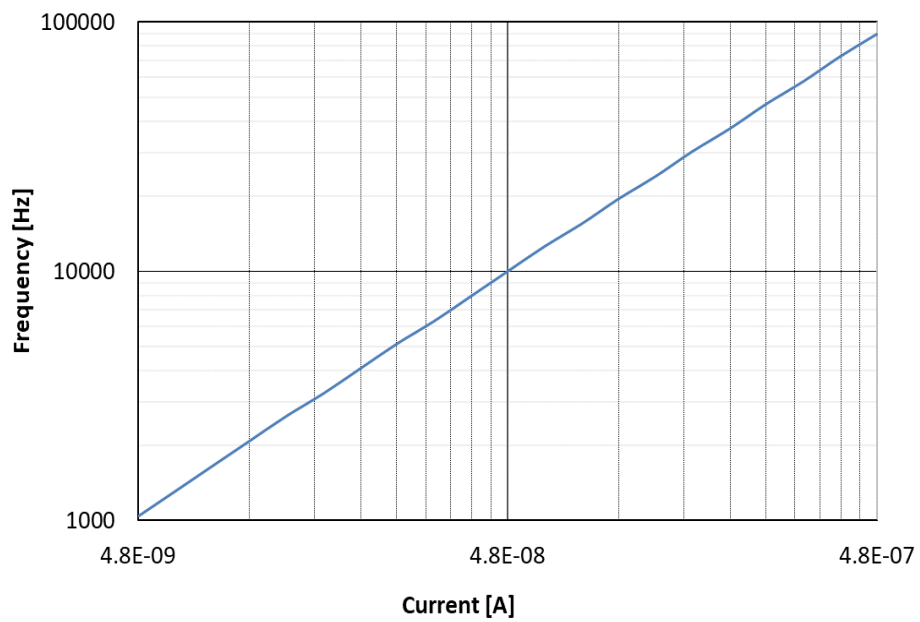


Figure 19: Center Frequency Vs. Bias Current Relationship Trendlin

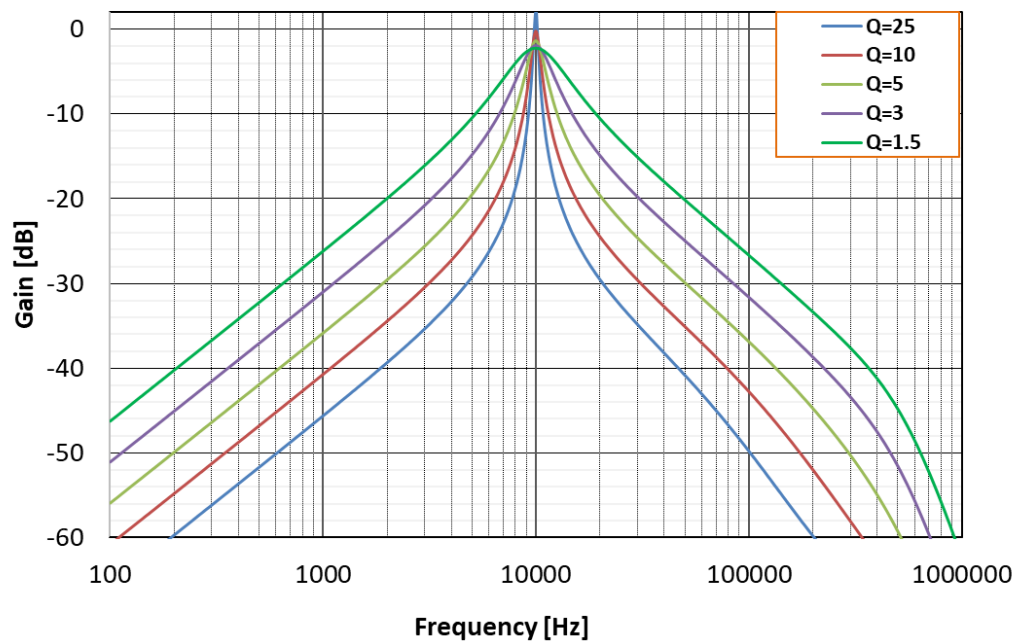


Figure 20: G_{m3} Current Bias Sweep Controlling Filter Q

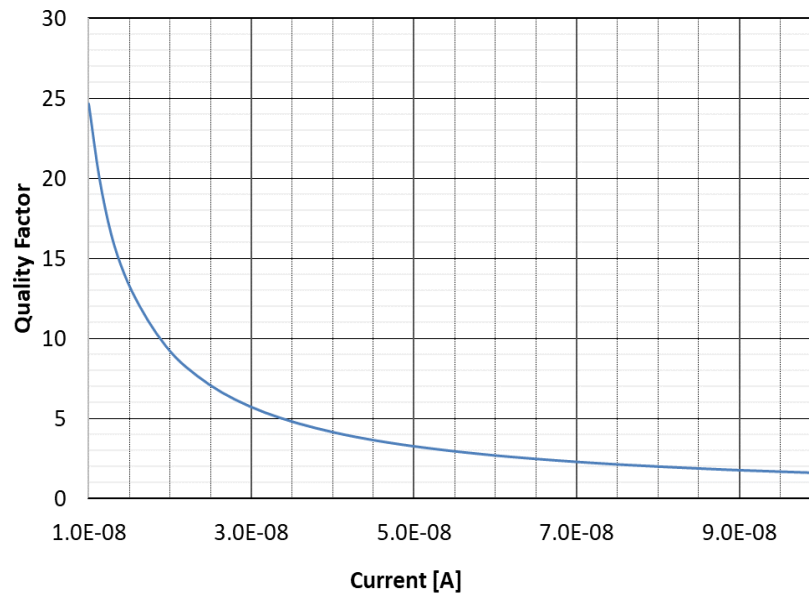


Figure 21: Quality Factor Vs. Bias Current Relationship Trendline

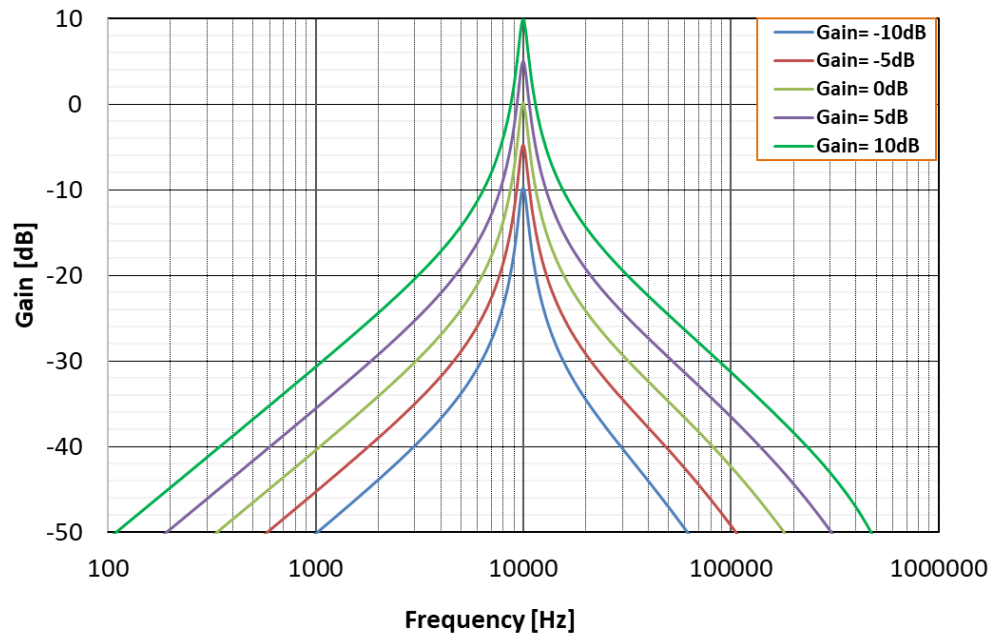


Figure 22: G_{m4} Current Bias Sweep Controlling Filter Gain

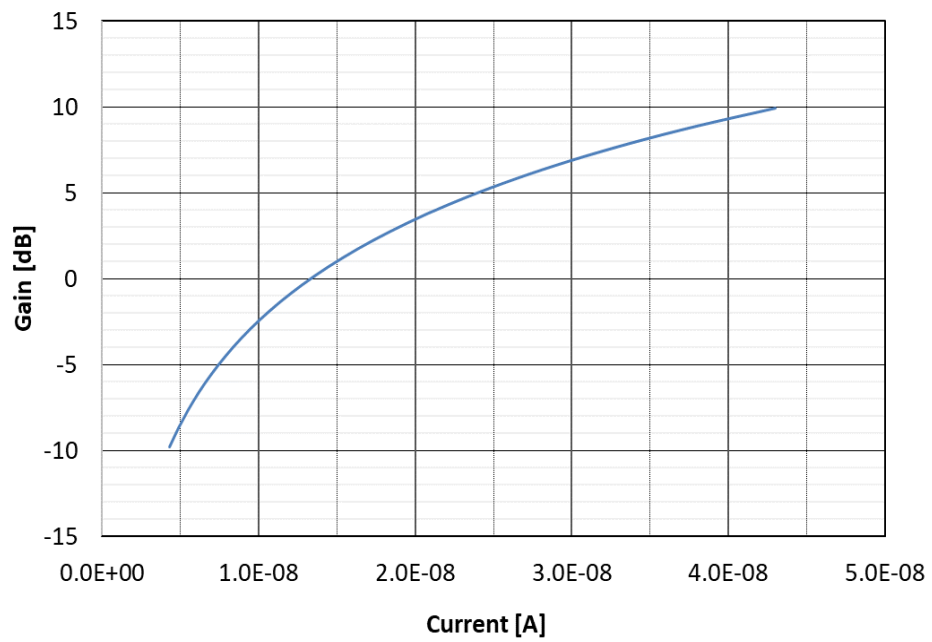


Figure 23: Gain Vs. Bias Current Relationship Trendline

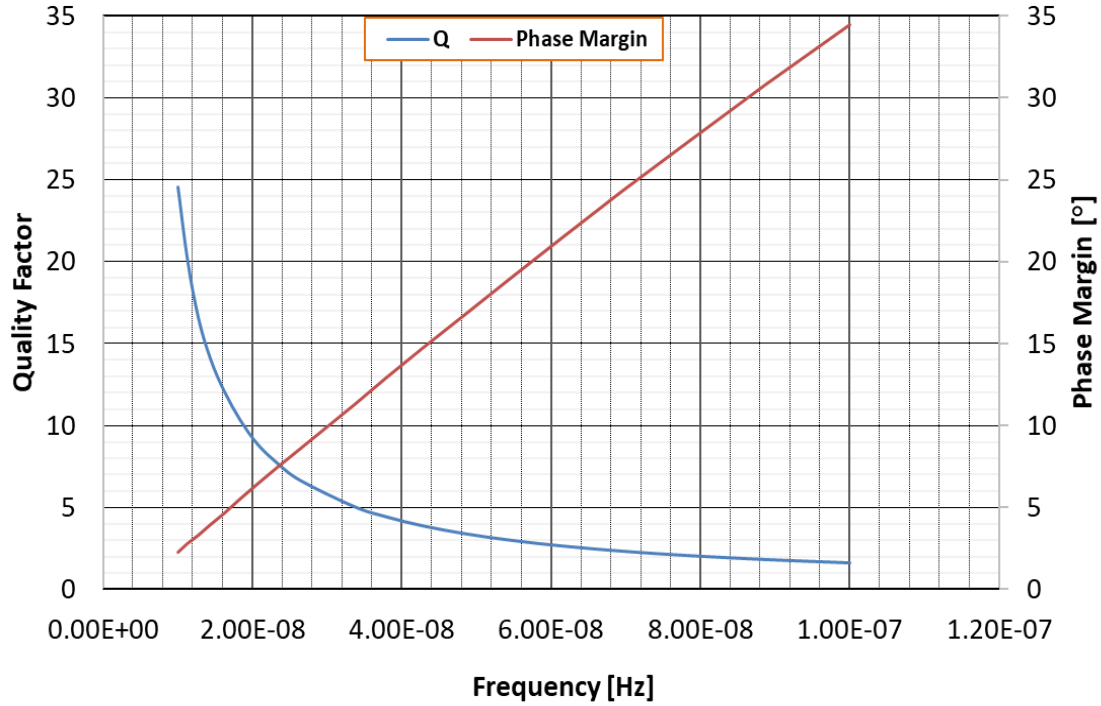


Figure 24: G_{m3} Bias Current Sweep Controlling Q and Phase Margin

Bias and Buffer Verification

Both the Minch current mirror and the Op-Amp buffer were simulated and verified for expected performance. The Minch current mirror schematic is illustrated below in Figure 25. The Minch current mirror [10] was chosen because of its optimal performance across a wide range of current levels including in the subthreshold region. The input stage of the mirror is a simple PMOS cascode current mirror that biases the rest of the circuit. Transistor M8 is sized much larger than the unit transistors because it acts as current-controlled voltage source that biases both M9 and M15 well above the saturation knee which is measured at about 100mV. From here M10 and M16 act like a Sooch current mirror [11] that replicate the saturation biasing to the output transistors. The current-voltage curve is plotted in Figure 26 with decreasing bias currents: 100nA, 10nA, and 1nA. The current gain is also displayed in Figure 27 where the input current is swept from

100pA to 1 μ A and the output current is measured with the worst current gain falling to 90% at lowest current setting, 100pA.

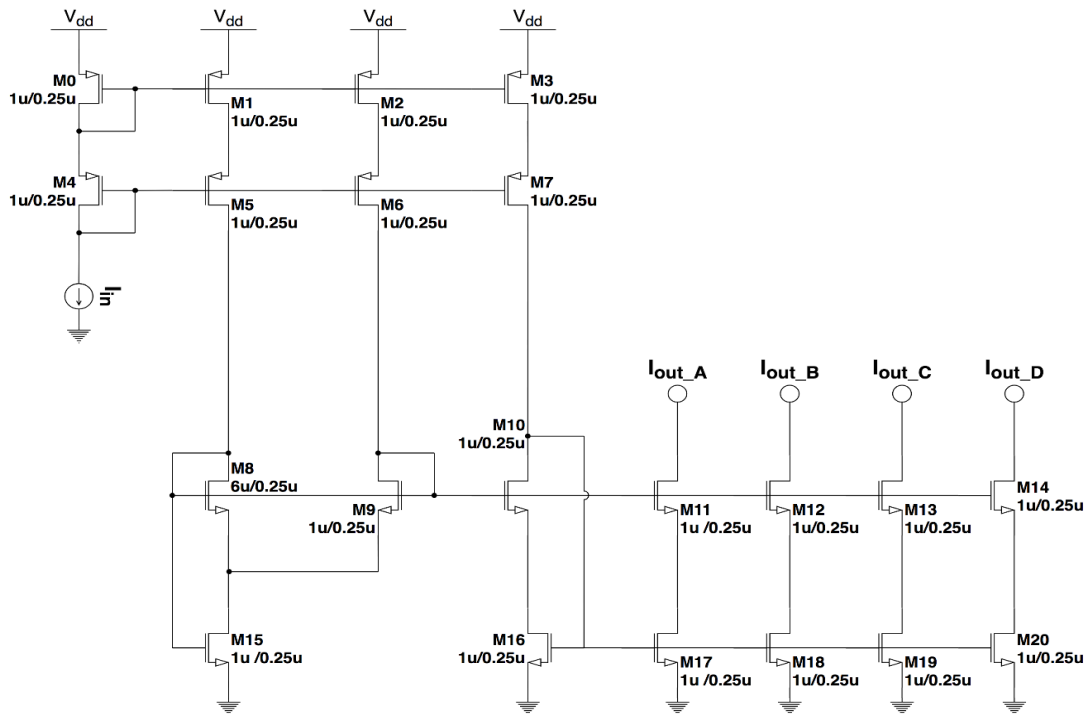


Figure 25: Minch Schematic

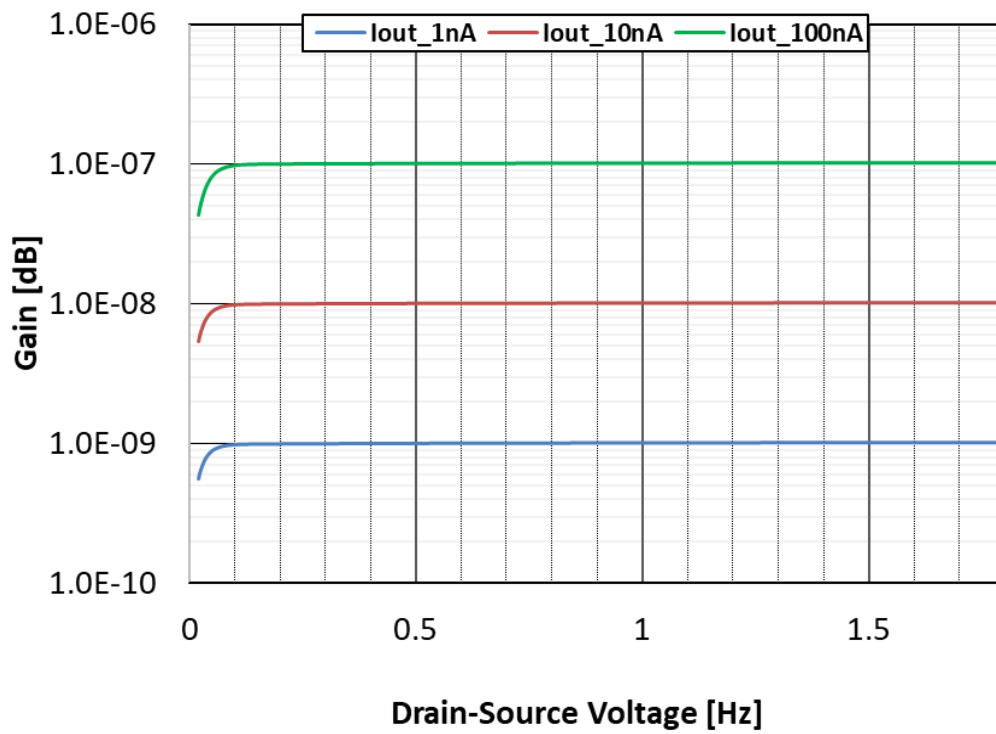


Figure 26: Minch I-V Curve for Bias Currents of 1nA, 10nA, 100nA, and 1uA

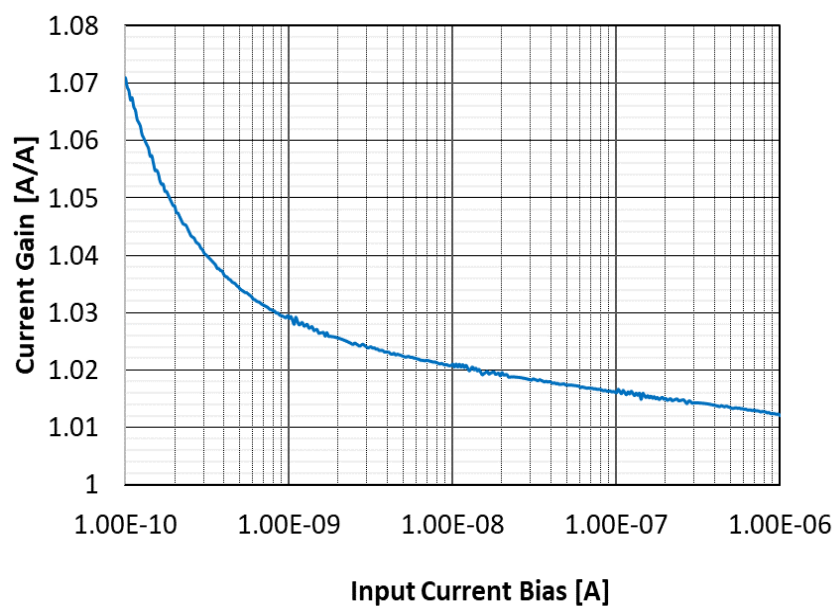


Figure 27: Minch Current Gain Sweep

The Op-Amp schematic is pictured below in Figure 28. The topology is a current biased input differential pair with a compensated Class AB output stage. The closed-loop simulation was conducted with the 100nA biased Op-Amp in unity gain configuration with a 10M Ω and a 15pF load. The closed-loop gain remains one until the cutoff frequency is reached at $\sim 600\text{kHz}$ as shown in Figure 29. The open loop simulation is conducted with the same load and bias with a DC feedback network. Figure 30 is a Bode plot showing an open-loop gain of $\sim 73\text{dB}$, a crossover frequency of $\sim 30\text{kHz}$, and phase at the crossover frequency of $\sim 89^\circ$.

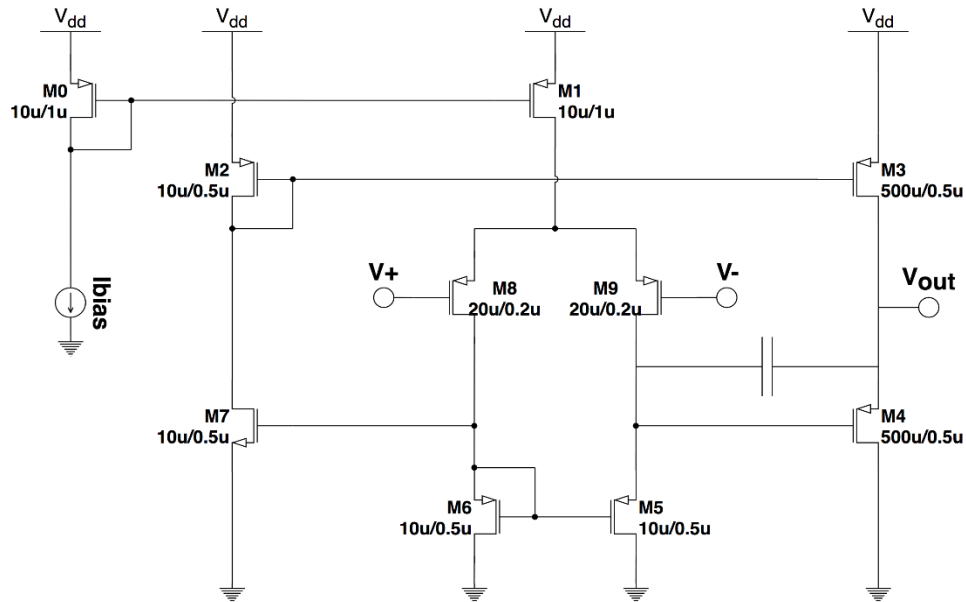


Figure 28: Op-Amp Schematic

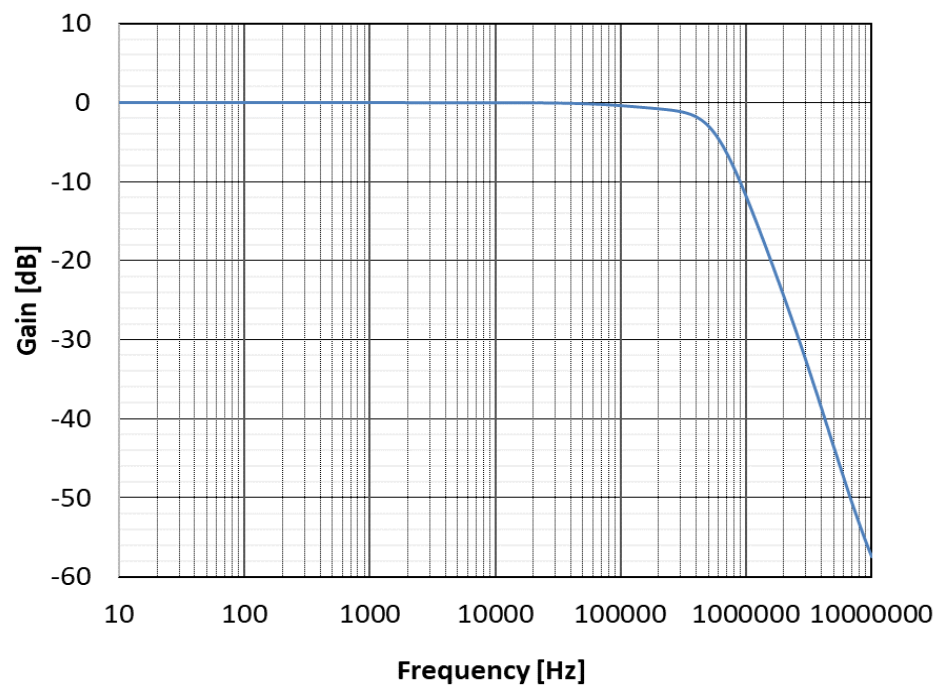


Figure 29: Op-Amp Closed-Loop Gain

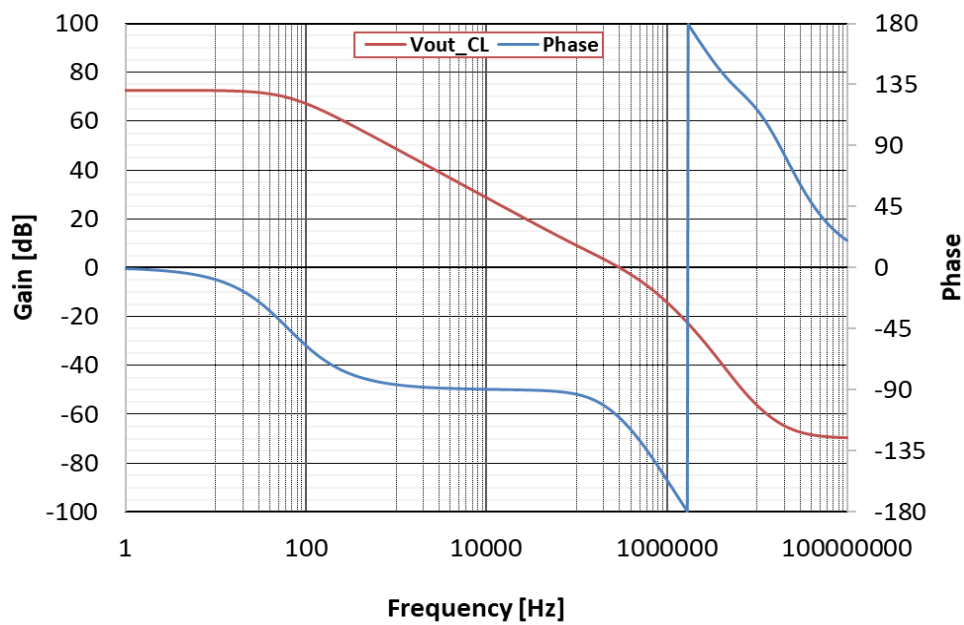


Figure 30: OTA Open-Loop Gain and Phase

System Verification

Following verification of Minch current mirror and the Op-Amp buffer designs, a full filter bank simulation was performed using four cascaded biquad filters as shown in Figure 31. The biquad filter bank simulation result of Figure 32 shows the increasing cascaded order response of the 2nd, 4th, 6th, and 8th-order outputs. This shows the performance advantage of cascading 2nd-order stages for to obtain improved passband and the rejection bands.

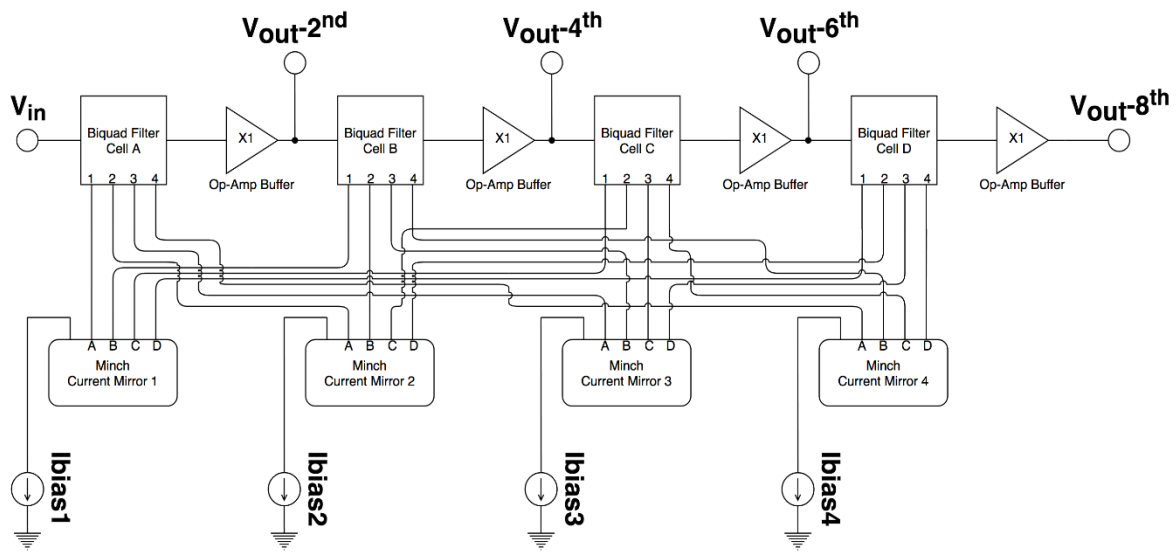


Figure 31: Schematic of Four Cascaded Biquad Filter Cells

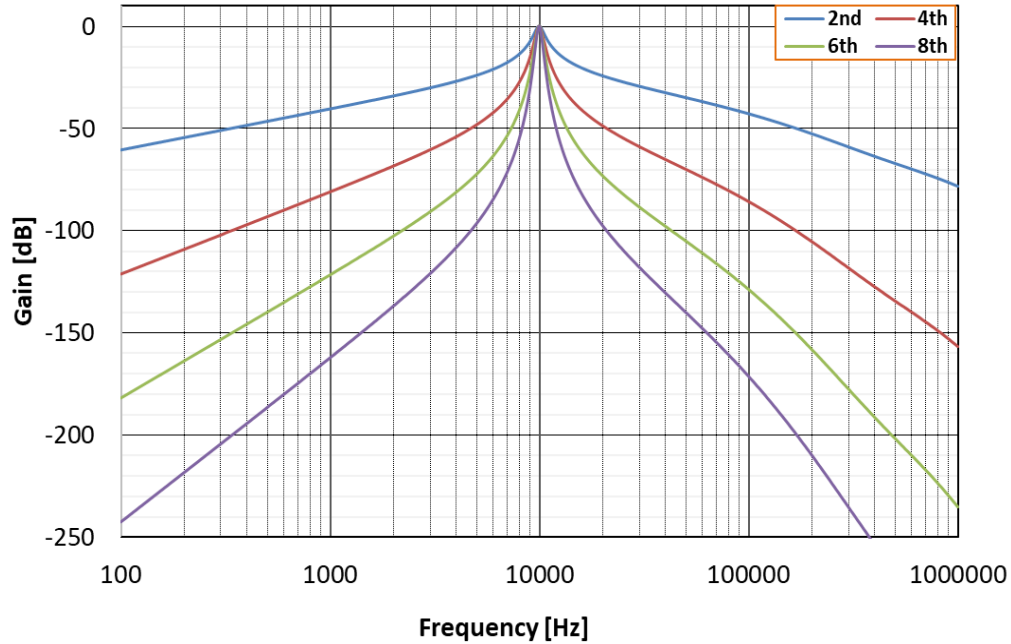


Figure 32: Plot of Biquad Filter Bank with 2nd-, 4th-, 6th-, and 8th-Order Responses

Physical Layout Design

Once all the circuit designs were verified using schematic level simulation, the physical layout of each cell was performed using Cadence Virtuoso Layout Suite XL. Each layout cell was verified using Mentor Graphics Calibre software and PDK provided rule decks: Design Rule Check (DRC) and Layout VS Schematic (LVS). Each hierarchy of designs was placed and routed until the top level was completed, and then placed and routed into a padframe with ESD protected pads. Fill materials were then added to the empty space and a seal ring was added to meet the fabrication foundry requirements. The completed chip layout (MISA2) was then submitted for fabrication.

Floorplan

Each integrated circuit must have a floorplan before tape-out to ensure all systems and circuits on the chips have been placed and routed correctly and efficiently. This planning ahead helps realize the full potential of the chip's area and pins. For the MISA2 tape-out, it was decided to floorplan the chip for 2 biquad filter channels, test OTA, test Op-Amp, and an unrelated experimental circuit design for another student in the bottom right side. The final layout can be viewed in Figure 33. The top array of biquad filters will be individually programmed for bias current and can optionally be externally cascaded. The biquad filter channel in the bottom left corner was internally cascaded with intermediate outputs and utilize programmed bias currents that are shared across the filter channel using the Minch current mirror.

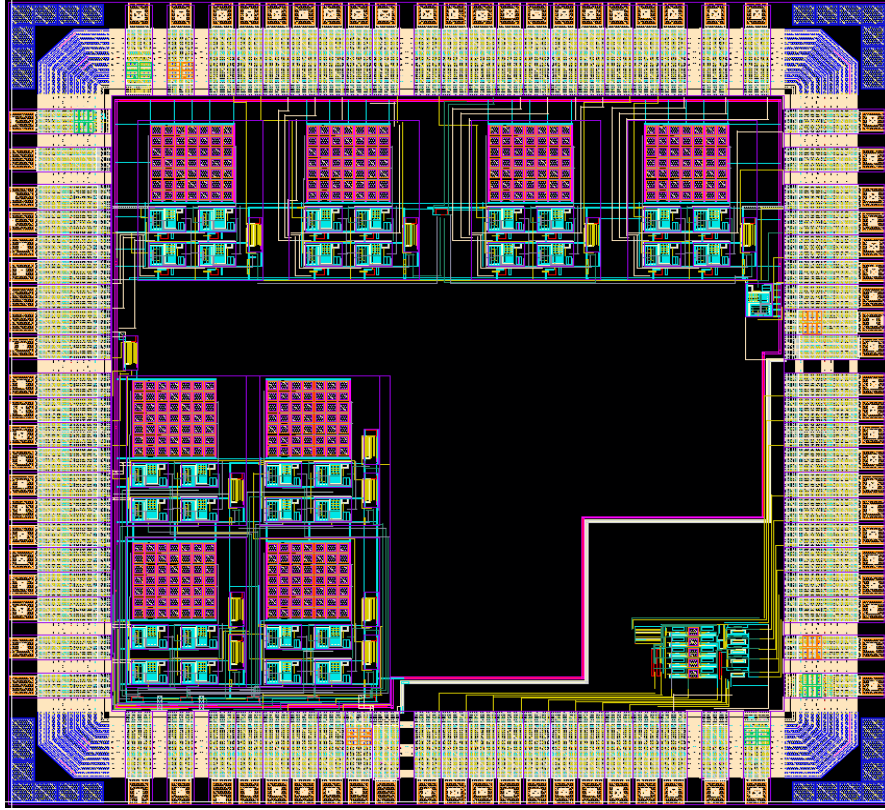


Figure 33: Layout of MISA2 Chip

Matching Requirements

The biquad channel requires very good matching in order to obtain the filter bank performance desired. Especially with high Q responses, mismatch between circuits can cause cascaded filter responses to be misaligned and deteriorate the composite filter bank response. Therefore, utmost care was taken in the layout of each biquad cell. Capacitors were implemented as multiple cell arrays using centroid optimization with dummy cells around the perimeter. The OTA and Op-Amp differential pairs were connected using the common centroid technique which reduces process mismatch significantly in both the x- and y-axis. While these layout techniques would help the biquad matching, there was one aspect that was

overlooked that would negatively affect the performance of the internally cascaded biquad filter channel. The mismatch of the Minch current mirror was quite large, mainly because of the use of short channel devices (250nm device lengths). Afterwards, Monte Carlo simulations were performed on the Minch current mirror with increasing channel length which clearly demonstrated their expected benefit (see Figure 34).

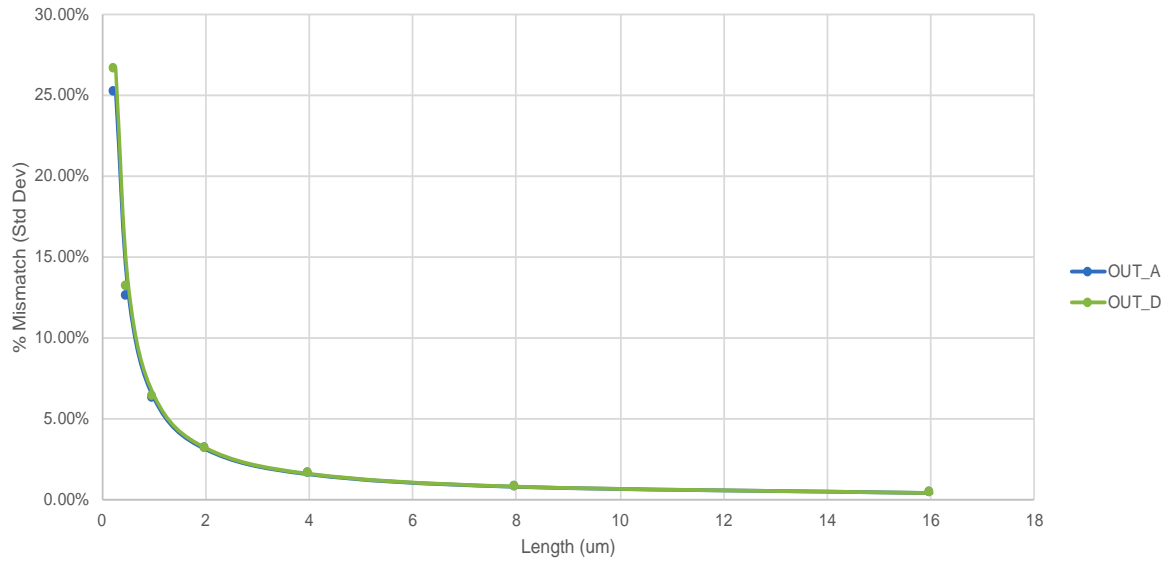


Figure 34: Monte Carlo Results of the Minch Current Mirror Mismatch Vs. Device Channel Length

CHAPTER FOUR

TEST RESULTS

Evaluation

The MISA2 chip design was fabricated in a 180-nm, 1.8-V CMOS process available through MOSIS. A microphotograph of the chip die, shown in Figure 35, provides an overview of the two groups of four biquad filter cells. One group (bottom left) was connected on-chip and shared a single set of bias currents, replicated by a local Minch current mirror cell. A second grouping of four biquad filters was also included on the chip (top grouping) with individual connectivity and bias currents that could be connected for off-chip cascading. Together, these two configurations allowed evaluation of the individual cells and externally connected cascaded cells up to 8th order (with individual biasing), as well as evaluation of 2nd to 8th order on-chip cascaded cells with shared biasing. These circuits enabled evaluation of the primary enhancements of Biquad filter over the MISA1 design, namely independent control of the Q and voltage gain. Other parameters of interest also include the programmed frequency range, power consumption, and matching. Other criteria evaluated include filter response shape, precision of digital programming, maximum obtainable quality factor and frequency settings, and noise levels.

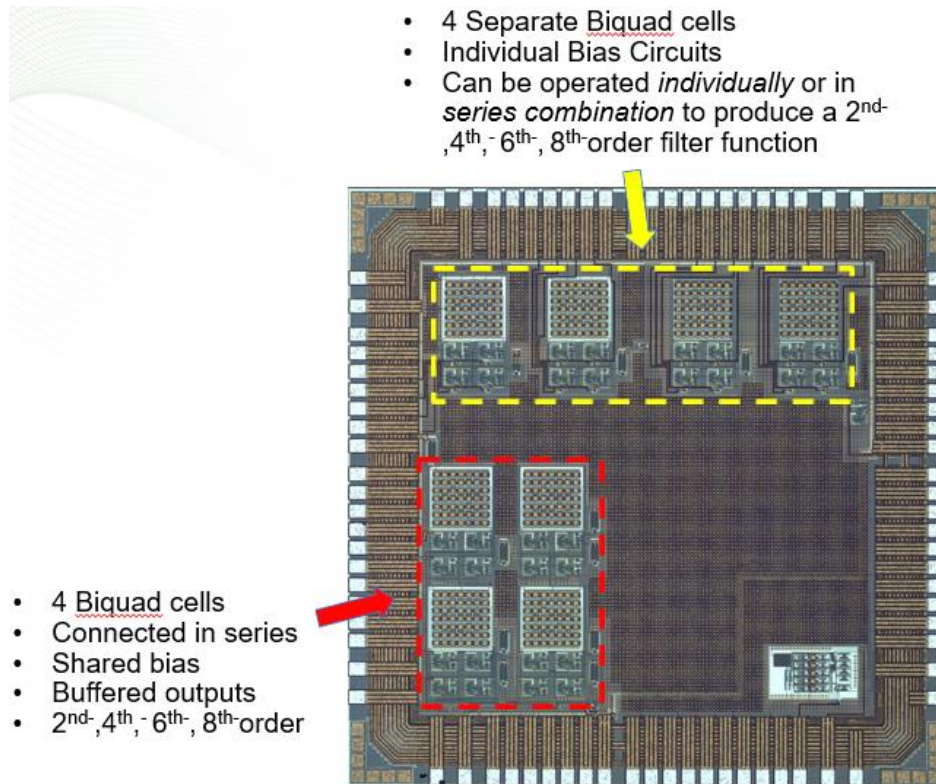


Figure 35: MISA2 Fabricated Chip

Testing Plan

In order to properly evaluate the design, a test plan was developed to focus our efforts on major criteria. The primary goal was to characterize the filter cell with different settings of frequency and Q. These filter response tests were performed on three chips to show the process variation for the die across the silicon wafer. With the 2nd-order response measured, the cascade channel was evaluated for the 4th, 6th, and 8th-order filter responses. Characterization of individual filter cells was necessary to evaluate general functionality and to assess the quality of matching between channels. While improved matching will enable practical use of the cascaded biquad filters at higher Q values than possible with MISA1 (MISA1 Q fixed at ~2.1), the addition of the extra current biases required for flexible Q control

made MISA2 significantly more complicated to program than its MISA1 predecessor. With the 2nd-order response measured, the cascade channel was measured for a 4th, 6th, and 8th-order filter responses. Figure 35 is a microphotograph of the fabricated chip and details the differences between the individual biquads at top and cascaded channel in the top left. Current bias differences were recorded for the separate filter channels. The programmed bias settings were given a quantifiable mismatch measurement between filter cells. These channels will be operated differently and individual biquad channels can be programmed to mitigate the effects of mismatch while the cascaded channel does not have this option. The power consumption was measured at the expected lowest and highest settings for an estimated nominal operation. Auxiliary measurements conducted determine the linear dynamic range and Total Harmonic Distortion (THD).

Printed Circuit Board

A test board was designed and fabricated to facilitate both full characterization of the MISA2 chip and use of the chip in a demonstration system. The PCB, pictured in Figure 36, facilitated testbed measurements for any individual biquad filter cell and has headers that can be shorted to form two cascaded 8th-order channels, or a single 16th-order system. Each main filter input or output is buffered on board with band-limited Sallen-Key circuits. Additional testing outputs will also utilize a simple Op-Amp buffer. Modification of the data acquisition software used for the MISA1 test system was performed to accommodate the eight current DACs required for the MISA2 filter chip biasing. Each DAC was programmed to output a voltage across a biasing resistor to generate the desired current using the regulated cascode stage (see Figure 37).

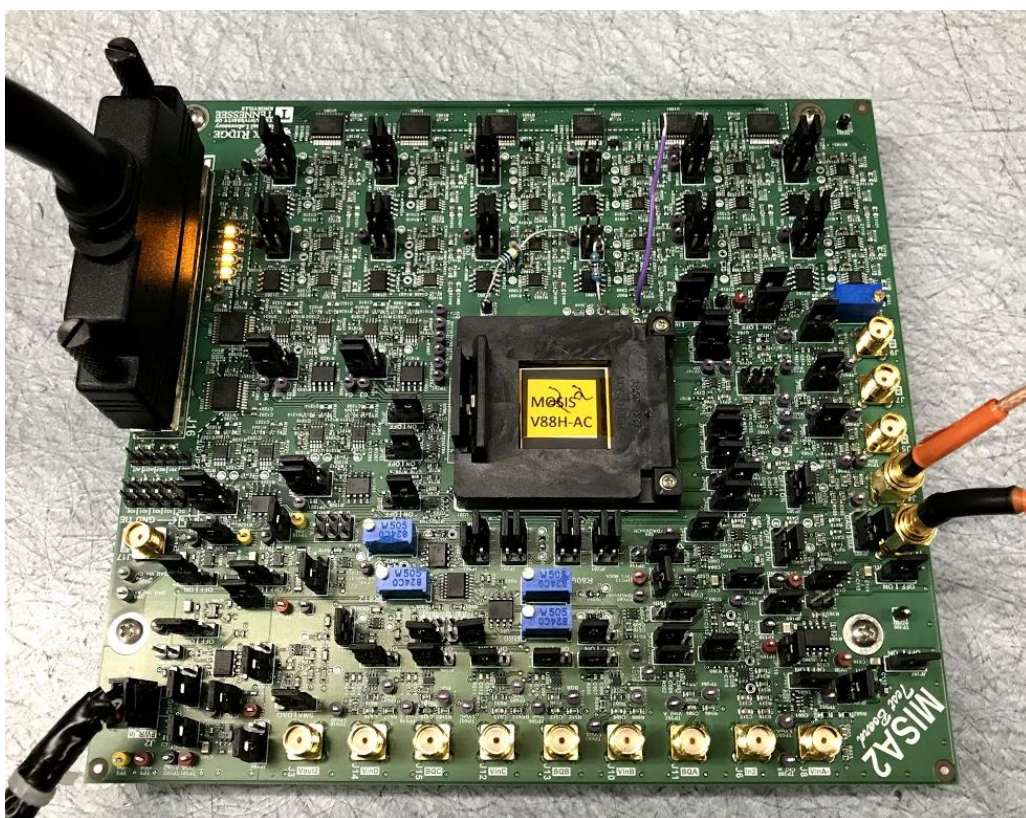
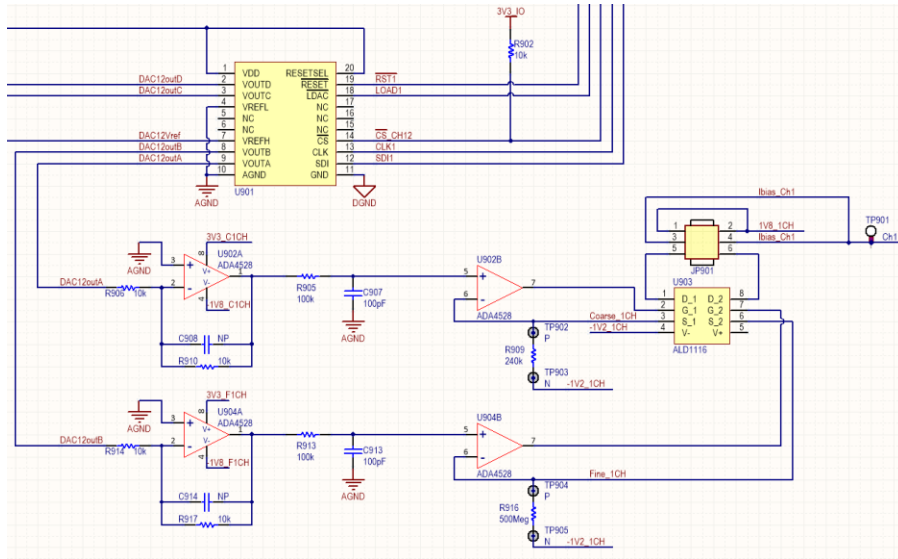


Figure 36: MISA2 Test Board



Equipment

Several pieces of equipment were used to conduct measurement of the MISA2 measurement system. The most important was the HP 3589A Spectrum/Network Analyzer which was used to measure the frequency response of the filter, and filter THD using an external stimulus (a Keysight 33500B Waveform Generator). A Keysight InfiniiVision MSOX4054A Mixed Signal Oscilloscope was used to measure the linear dynamic range and for board level troubleshooting. A Keithly 6430: Sub-Femtoamp Remote SourceMeter enabled very accurate low-current measurement, and a Fluke 787: Digital Multi-Meter was use for voltage and resistance measurements. The test board and MISA2 chip were powered using an Agilent E3648A 8W/50W Dual Output DC Power Supply. Finally, the digital programming of the filter test system was performed using an Agilent U2531A Data Acquisition unit with a HP Elitedesk computer running Windows 7 operating system and LabVIEW software.

Measurements

Filter Response

The first measurement conducted was the filter response of a 2nd-order biquad filter cell programmed at 10kHz, which is the middle of the frequency range. Figure 38 shows this filter response at low (5), normal (10), and high (20) quality factor settings. The individual biquad channel was programmed such that each individual filter cell center frequency aligned precisely producing an 8th-order, cascaded filter response pictured in Figure 39, shown with increasing spectral selectivity (Q=5, 10 and 20). These measurements verified the successful operation of the high Q biquad filter cell and the cascaded filter bank system. The true test was the comparison of the MISA1 16th-order filter channel. In Figure 40, the MISA2 intermediate outputs (2nd, 4th, 6th, and 8th order responses) were programmed for a center frequency of 10kHz and Q=10, and are plotted with the MISA1 16th-order filter for comparison. The 2nd-order biquad surpasses the effective quality factor of MISA1, but the response sidebands are limited to -40dB after a decade of frequency, whereas MISA2 response falls to the noise floor after only an octave of frequency. However, the 6th-order biquad filter response surpasses the MISA2 filter significantly in both cases. Figure 41 also presents a comparison of the MISA2 8th-order and MISA1 16th-order and is accompanied with a two-octave zoomed version. These tests verify the significant improvement in frequency selectivity obtained by MISA2 over MISA1, at much reduced filter order.

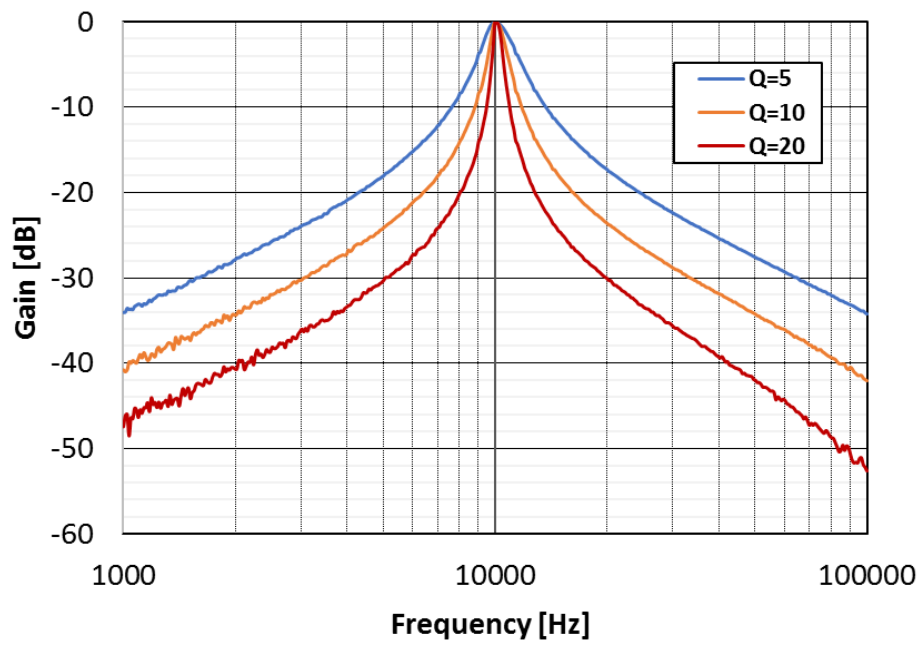


Figure 38: 2nd-Order 10kHz Biquad Filter for $Q=5, 10$, & 20

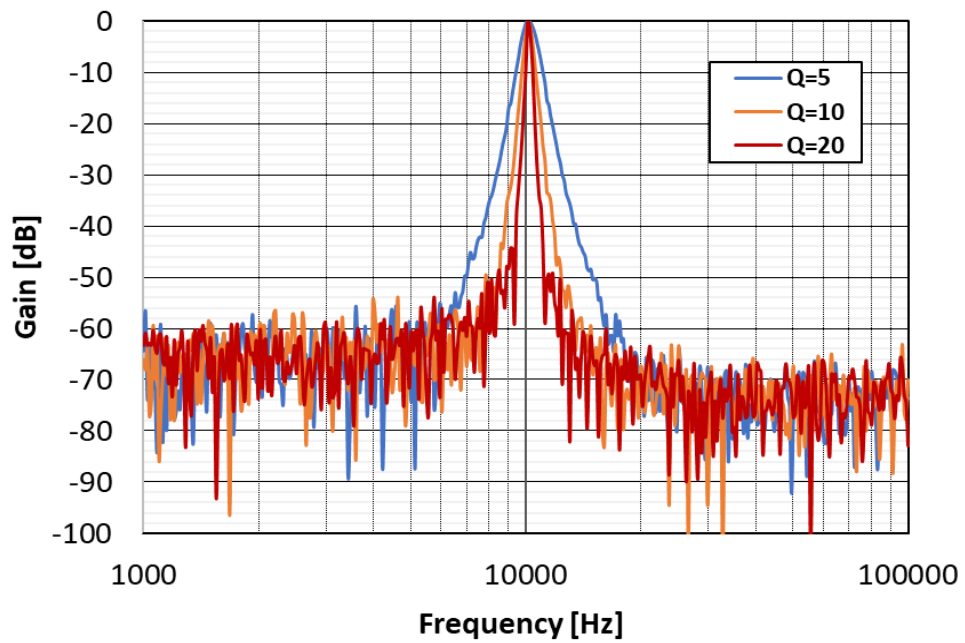


Figure 39: 8th-Order 10kHz Biquad Filter for $Q=5, 10$, & 20

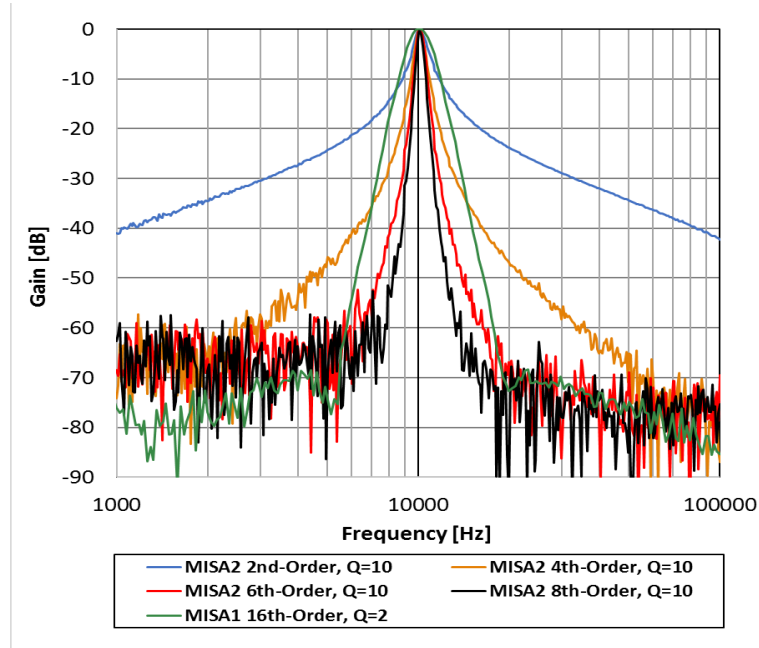


Figure 40: Comparison of the Measured 2nd-, 4th-, 6th-, 8th-Order Biquad Filters and the MISA1 16th-Order Filter

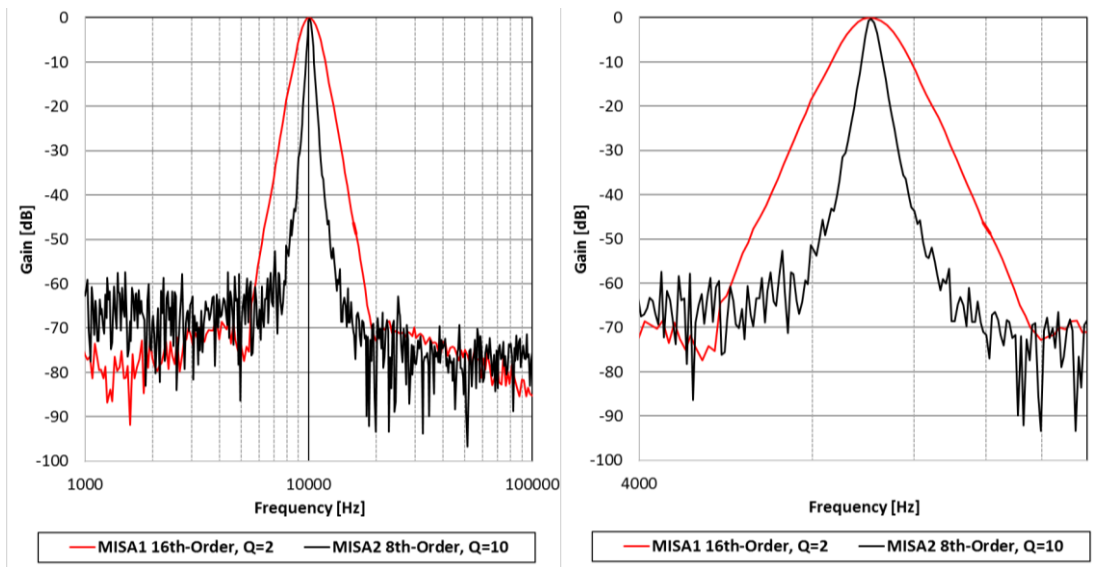


Figure 41: Normal (Left) and Zoomed (Right) Views of the 8th-Order Biquad Filter and the MISA1 16th-Order Filter Measured Frequency Response

Spectral Sweep

The filter response measurements confirmed successful realization of higher Q filter cells with digital control of the filter's selectivity. Now the filter could be programmed to sweep across the target spectrum. The 2nd-order filter response settings for 1kHz with increasing Q is presented below in Figure 42. The 8th-order filter response for 1kHz with increasing Q is shown in Figure 43. An interesting note is the observed sensitivity for the 1kHz center frequency, especially for the 8th-order response. Programming settings for the 1kHz response was difficult because of the limited digital resolution and the noise sensitivity of the filter, caused by the very small biasing current required (in the sub-nanoamp range). The 100kHz center frequency settings did not exhibit this sensitivity issue since it was programmed with a much larger current bias. The 2nd-order response and 8th-order response for the 100kHz setting with increasing Q are plotted below in Figure 44 and Figure 45 respectively.

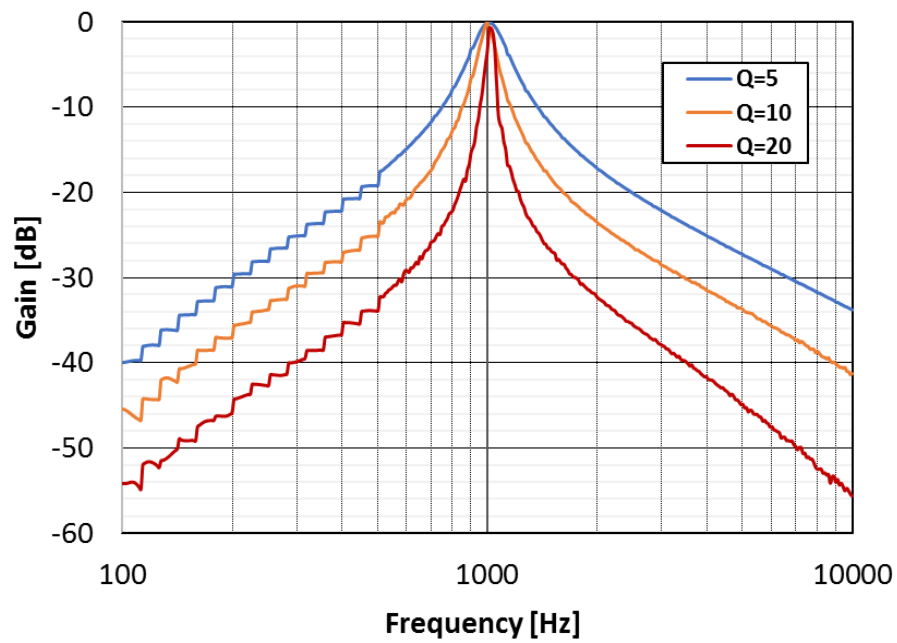


Figure 42: 2nd-Order 1kHz Biquad Filter with Varying Q=5,10, & 20

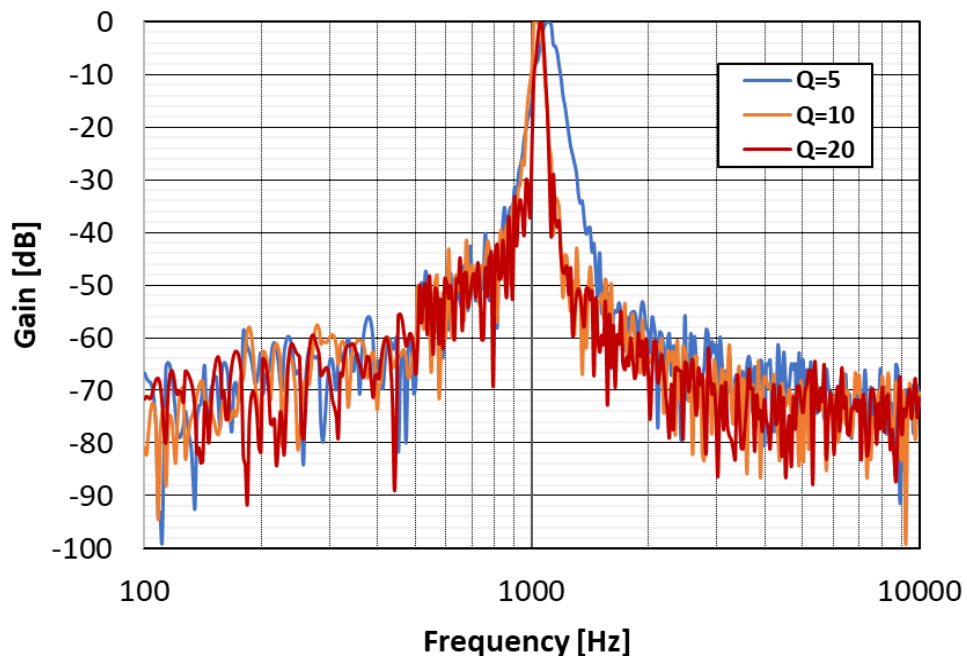


Figure 43: 8th-Order 1kHz Biquad Filter with Varying Q=5,10, & 20

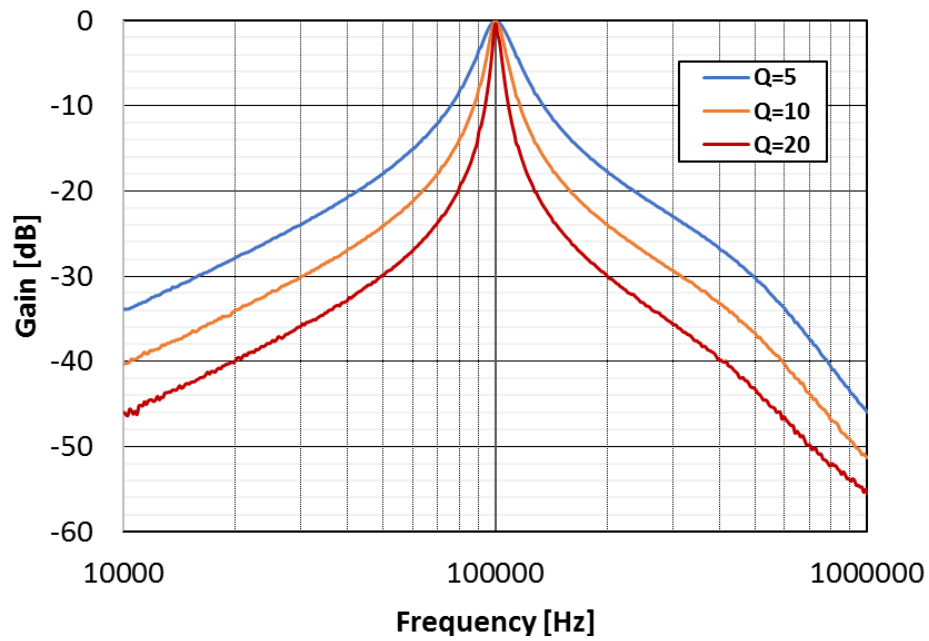


Figure 44: Gain Normalized 2nd-Order 100kHz Biquad Filter with Varying Q=5,10, & 20

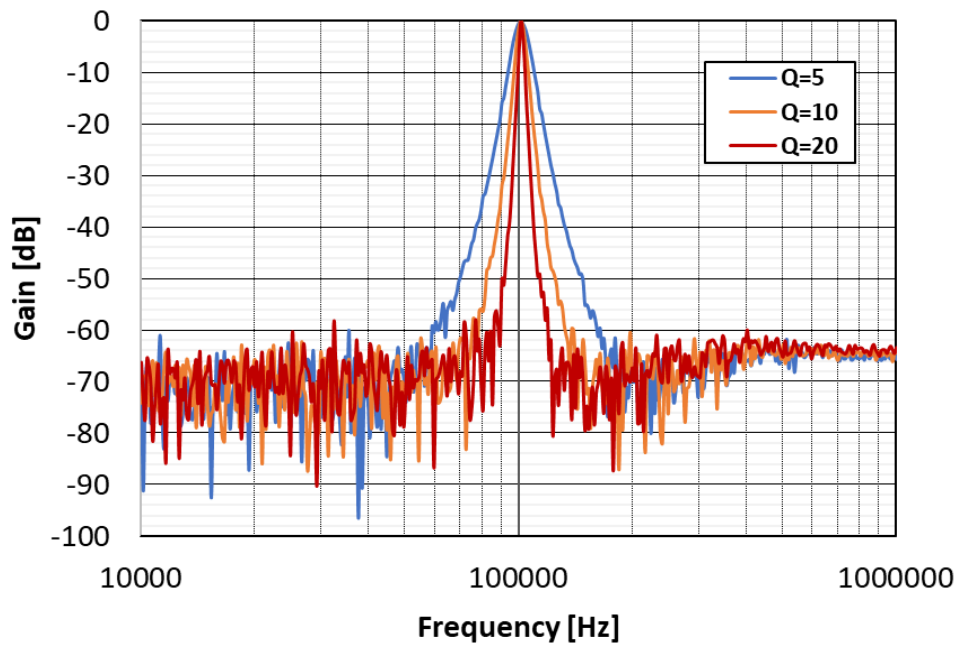


Figure 45: Gain Normalized 8th-Order 100kHz Biquad Filter with Varying Q=5,10, & 20

Overall, the spectral sweeps of the Biquad filter fully satisfied the requirements. To better understand its limitations, the Biquad filter was also programmed for a 500kHz center frequency, as shown in Figure 46. At this higher frequency limitations begin to reveal themselves. A right-half plane zero can be observed near 4MHz. While this did not affect normal operation of the filter it would need to be addressed for higher frequency operation.

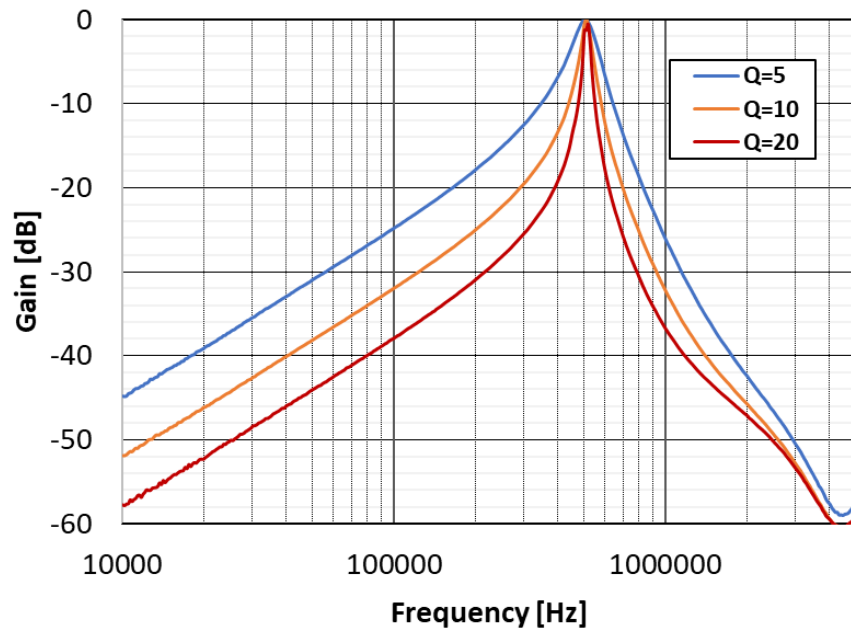


Figure 46: 2nd-Order 500kHz Biquad Filter with Varying Q=5,10,& 20

Power Consumption

Because of its remote sensing platform applications, it is very important that the filter system consume very little power enabling long dwell times on a battery-based power source. The required power consumption was desired to be less than $155\mu\text{W}$ for an 8th-order filter. This measurement verifies the completion of this requirement as seen in Table 1. Power consumption is directly proportional to the center frequency of the filter, thus at the highest required frequency, 100 kHz, the consumed power is $108\mu\text{W}$. The dwell time for this circuit can be estimated using a standard alkaline battery (2500mAh) as a power source. For the worst-case operation at 100 kHz, the dwell time would be 41,667 hours or ~4.75 years. At nominal operation, average consumed power for all frequency settings, the dwell time would be 56,606 hours or ~6.5 years.

Table 1: Power Consumption of Biquad Filters across Frequency Spectrum

Frequency	2nd-order	8th-order
1kHz	$12.9\mu\text{W}$	$51.7\mu\text{W}$
100kHz	$27\mu\text{W}$	$108\mu\text{W}$
500kHz	$112\mu\text{W}$	$448\mu\text{W}$ *Not measured

Harmonic Distortion Analysis

The Total Harmonic Distortion (THD) was measured by driving the Biquad filter with a low-distortion sine wave and measuring the spectrum output of the filter plotted in Figure 47. THD was then calculated by converting the harmonic peaks to voltage units and summing the Root-Mean-Square [RMS] of the harmonics divided by the fundamental as seen in Equation 10.

$$THD = \frac{\sqrt{V_1^2 + V_2^2 + V_3^2 + V_4^2 + \dots}}{V_0} \quad Eq. (10)$$

This THD measurement was conducted for both the 2nd-order and the 8th-order response for the 10 kHz center frequency and Q=10 settings. The input signal amplitude was also swept to analyze the relationship to THD. This allowed for a comparison of the 2nd-order and the 8th-order responses for THD versus the input amplitude (see Figure 48). Interestingly, the THD of the 8th-order response saturates to 1.5%, whereas the 2nd-order continues to increase with input amplitude. This is likely due to the very high Q or narrow passband of the filter that suppresses the harmonics. When cascaded, following stages may further suppress the harmonics and prevent mixing that would normally contribute to the growth of higher harmonics, such as the 4th and the 5th harmonics with increasing input signal amplitude. With more cascaded filter stages, the higher frequency harmonics are stabilized since the 8th-order response has a stopband below the noise floor. This is the reasoning for the saturated THD curve for 8th-order filter for increasing input signal amplitude.

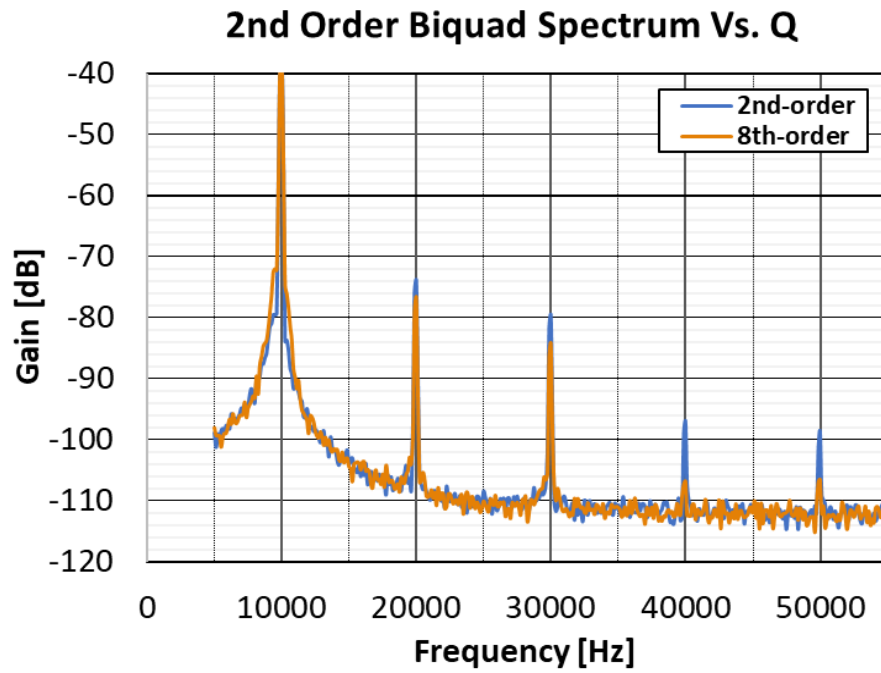


Figure 47: MISA2 Measured THD Spectrum of Both 2nd- and 8th-Order Filters

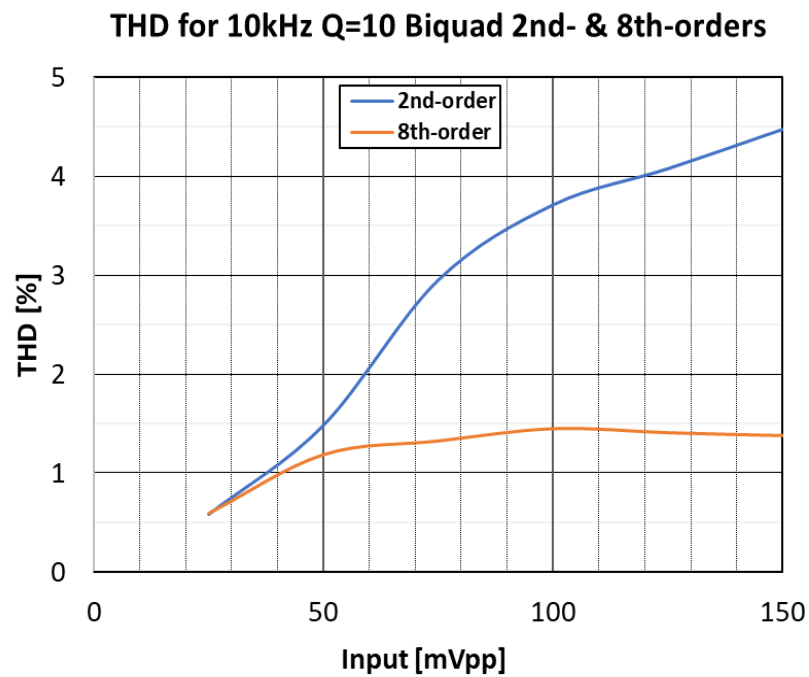


Figure 48: THD Comparison between 2nd- and 8th-Order Response for Increasing Input Amplitude

Linear Range

The linear dynamic range [LDR] is where the gain of a circuit begins to compress with increasing input signal amplitude. This is where the assumption of small-signal analysis no longer holds and the circuit components may no longer function linearly. This small-signal boundary is important because it determines the maximum input signal upper boundary of the Signal-to-Noise Ratio [SNR]. The SNR is a common benchmark for circuits and system that quantifies the logarithmic amplitude level between the signal of interest and noise sources that may interfere with the quality of signal processing, reception, or transmission. While gain can be added later in a signal path to boost the amplitude, it will also amplify the noise. Therefore, SNR is an important specification since it is a fixed ratio generally determined by the first stage of a system. The LDR of the filter cell was limited by the differential input linear range of OTA and any internal nodes that may have voltage gain. The capacitor ratio is the primary reason for the internal voltage gain on the filter cell. However, this capacitor ratio also defines the filter's Q. The value of this capacitor ratio is a trade-off between the filter linear range selectivity. The LDR was measured by setting the gain of the filter to a known value, in this case 0dB, and the input sinusoid was increased beyond the point that the filter gain begins to compress. The LDR was measured for both a low Q (5), shown in Figure 49, and high Q (20), shown in Figure 50, both at 100 kHz for a 2nd-order biquad filter response.

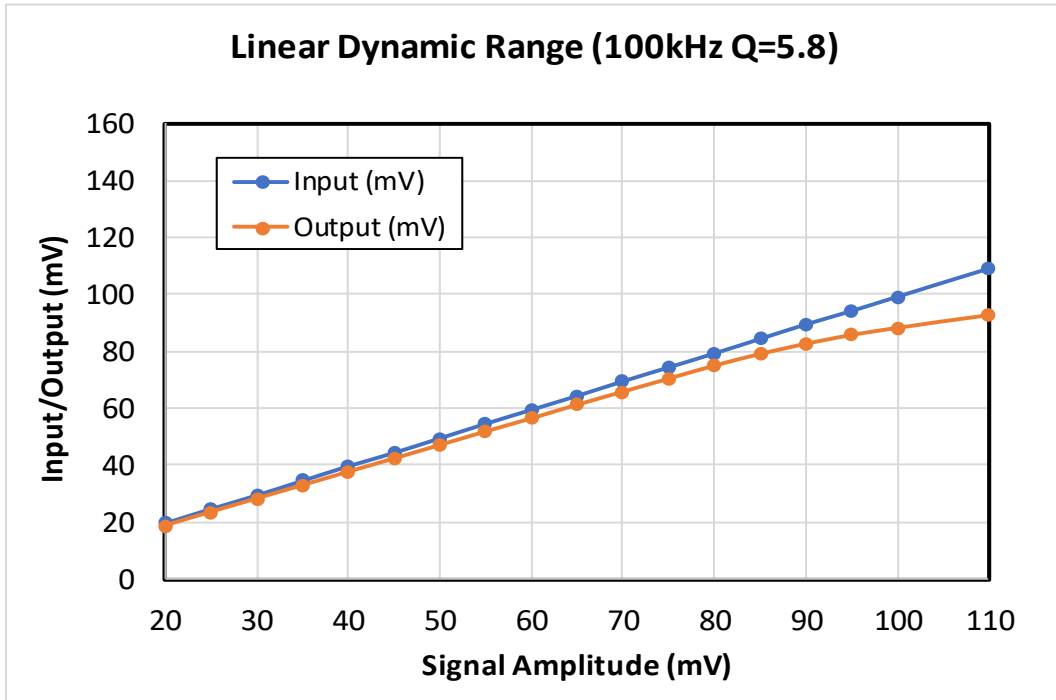


Figure 49: MISA2 Linear Dynamic Range for Low Q=5

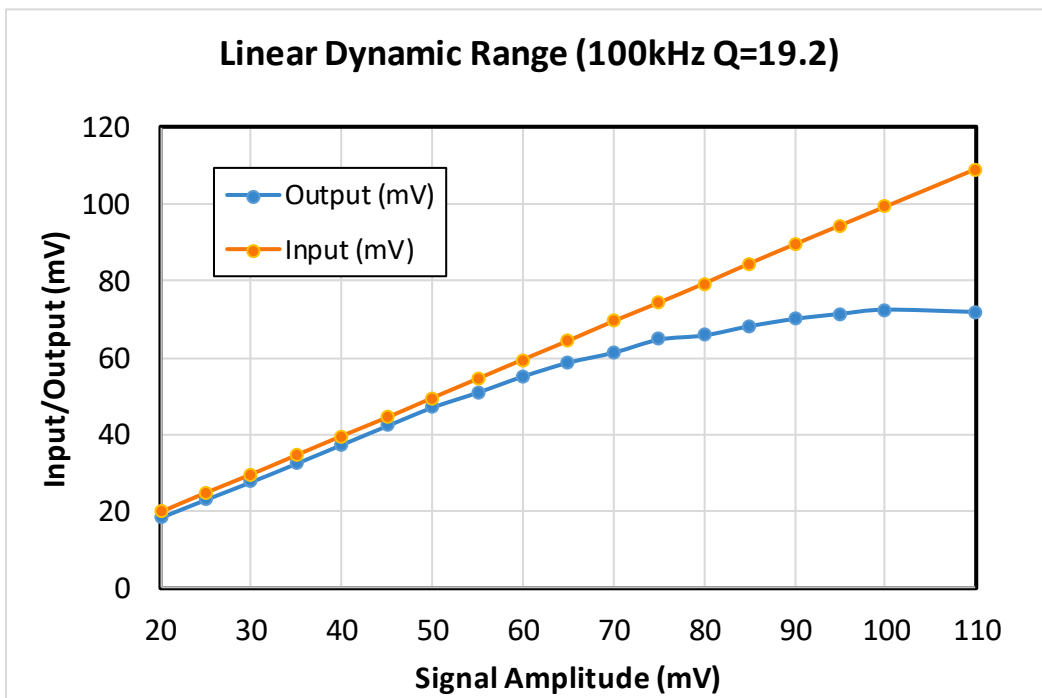


Figure 50: MISA2 Linear Dynamic Range for High Q=20

Matching Performance

The matching between biquad filters was very important for successful cascading of stages with high quality factor. Several steps were taken to reduce mismatch of the differential pair transistors and capacitors. Common centroid layout technique and dummy cells were both leveraged to reduce mismatch. Long length devices were used in the biquad to prevent mismatch and short-channels effects.

One important section that was overlooked was the Minch current mirror section. This was confirmed as the main source of mismatch by examining the Monte Carlo simulations and measuring the current output mismatch for both the MISA1 and MISA2 chips. Monte Carlo analysis was conducted on this circuit with varying unit transistor lengths and these results were examined previously in Figure 34. Both chips (MISA1 and MISA2) were fabricated with the same Minch current mirror design having a unit transistor width of $1\mu\text{m}$ and length of $0.25\mu\text{m}$. The current mismatch for the MISA1 chip was measured at four different bias circuits and five chips as shown in Table 2. The current mismatch was also measured for the MISA2 chip at four separate bias circuits and three chips as shown in Table 3. The MISA2 measured current mismatch could vary 30% below or above the input bias current. This had a detrimental effect on the channel of Biquads with shared biasing and internally cascaded sections. Figure 51 demonstrates how each stage was biased differently and thus reduced the spectral performance of the filter with each additional stage (note that these Biquads were programmed to 10 kHz and $Q=5$).

Table 2: MISA1 Minch Current Mirror Measured Mismatch

MISA1 Minch	Chip1 % Mismatch	Chip2 % Mismatch	Chip3 % Mismatch	Chip4 % Mismatch	Chip5 % Mismatch
Op-Amp Bias	-25.9%	+12.7%	+30.4%	+6.4%	-9.7%
I _L Bias	-34.4%	+7.7%	-30.1%	+10.6%	-1.3%
I _H Bias	-10.8%	+1.3%	+11.2%	+33.5%	+9.5%
Source Follower Bias	+8.7%	-3.0%	+19.5%	+20.2%	-10.1%

Table 3: MISA2 Minch Current Mirror Measured Mismatch

MISA2 Minch	Chip2 % Mismatch	Chip3 % Mismatch	Chip4 % Mismatch
I _{bias1}	-11.54%	-13.8%	+28%
I _{bias2}	-16.6%	+1.06%	-11.4%
I _{bias3}	+18.1%	+21.1%	-23.1%
I _{bias4}	-36.2%	+10.7%	-20.7%

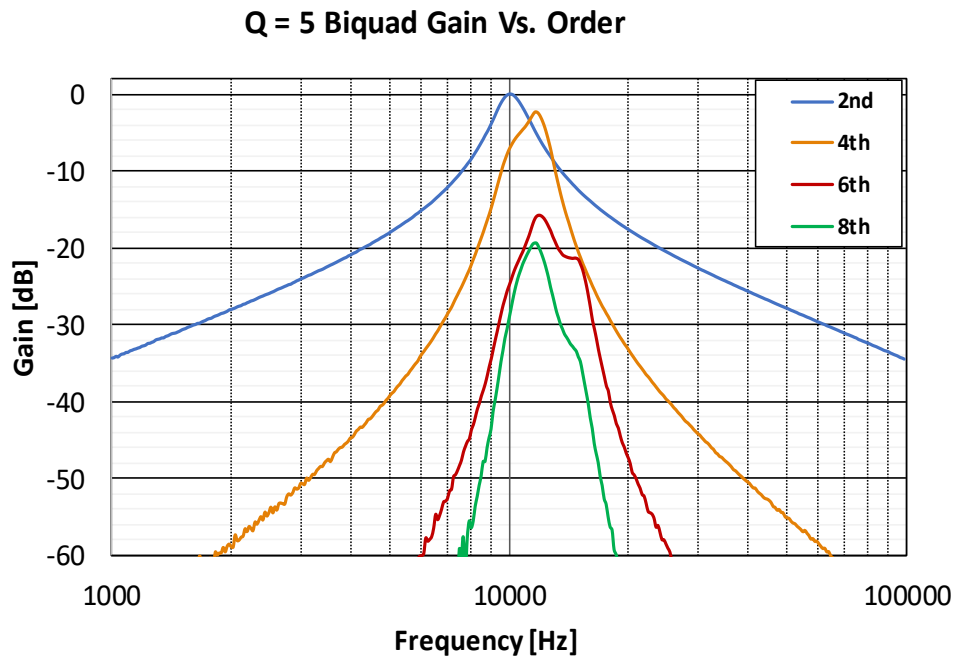


Figure 51: Shared Bias Channel Biquads with Q=5 Demonstrates Mismatch Effects on Cascaded 2nd-Order Filters

The transfer function of several chips were measured to evaluate the process variation for different die. The shape of filter response is compared for a programmed frequency, while the difference in bias currents are recorded and compared later. Significant variation was observed for the 1kHz 2nd-order response (Figure 52) and the 8th-order response (Figure 53). This particular setting is very sensitive to environmental noise associated with low bias current levels. The 10kHz setting demonstrates a much more robust response for the 2nd-order and 8th-order as seen in Figure 54 and Figure 55, respectively. This is also true for the 100kHz setting seen in Figure 56 and Figure 57.

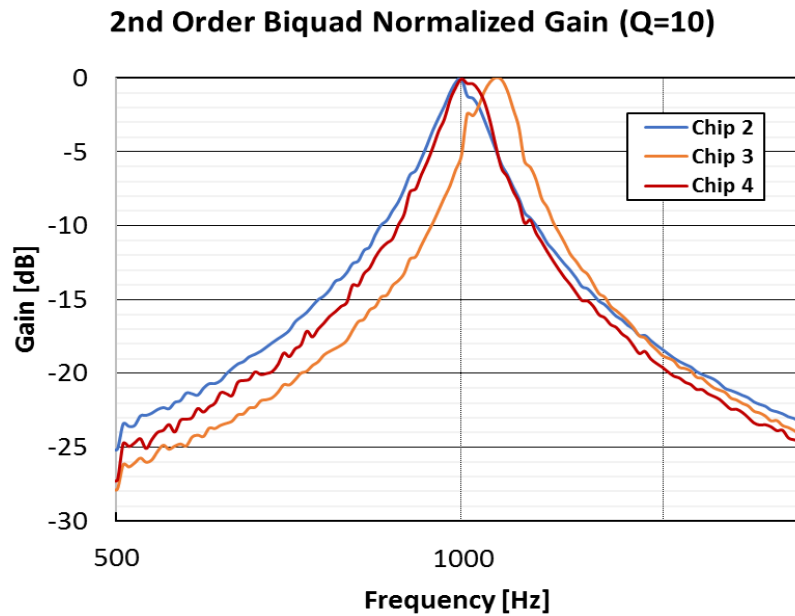


Figure 52: Zoomed 2nd-Order 1kHz MISA2 Biquad Filter of Three Chips

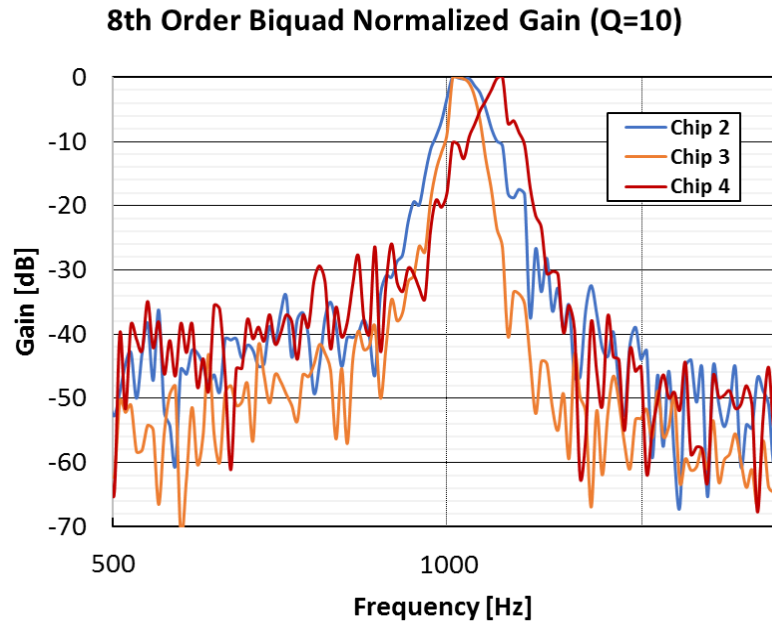


Figure 53: Zoomed 8th-Order 1kHz MISA2 Biquad Filter of Three Chips

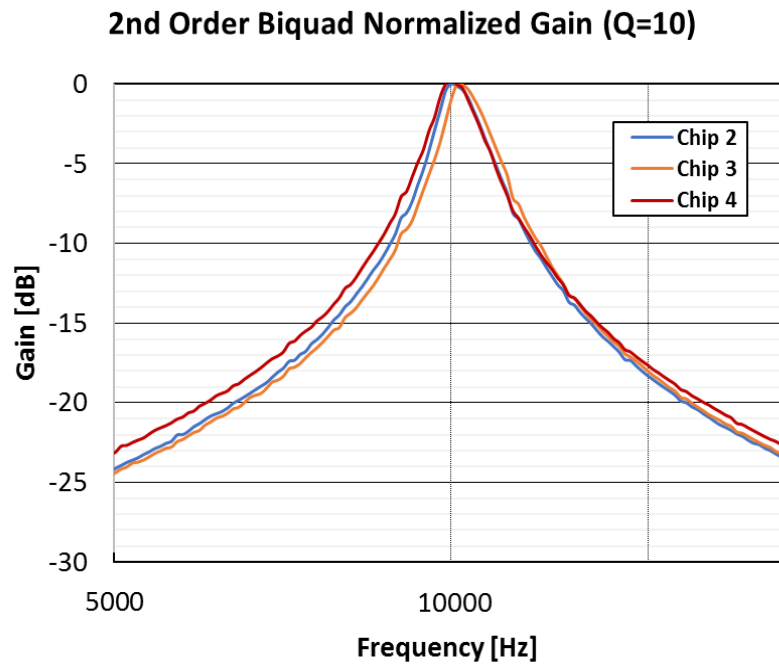


Figure 54: Zoomed 2nd-Order 10kHz MISA2 Biquad Filter of Three Chips

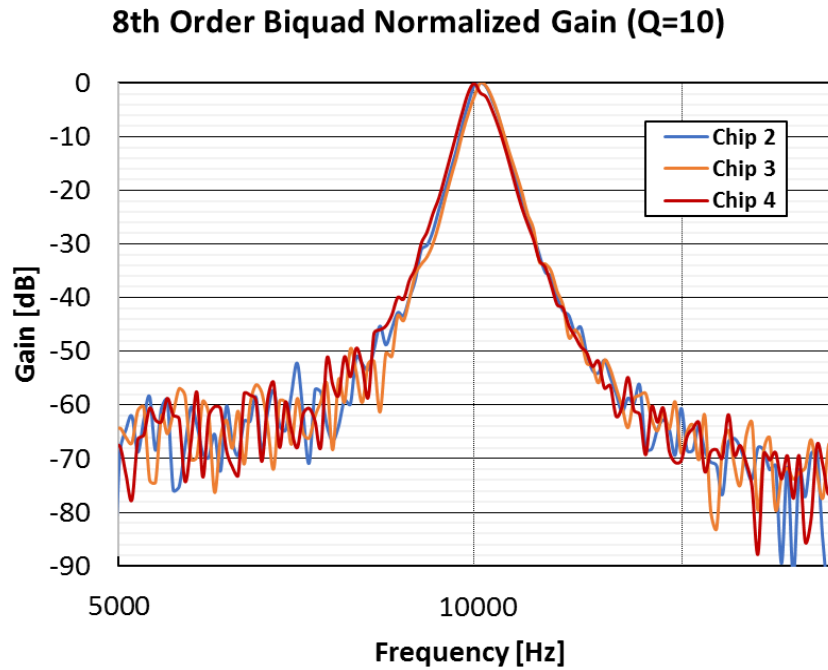


Figure 55: Zoomed 8th-Order 10kHz MISA2 Biquad Filter of Three Chips

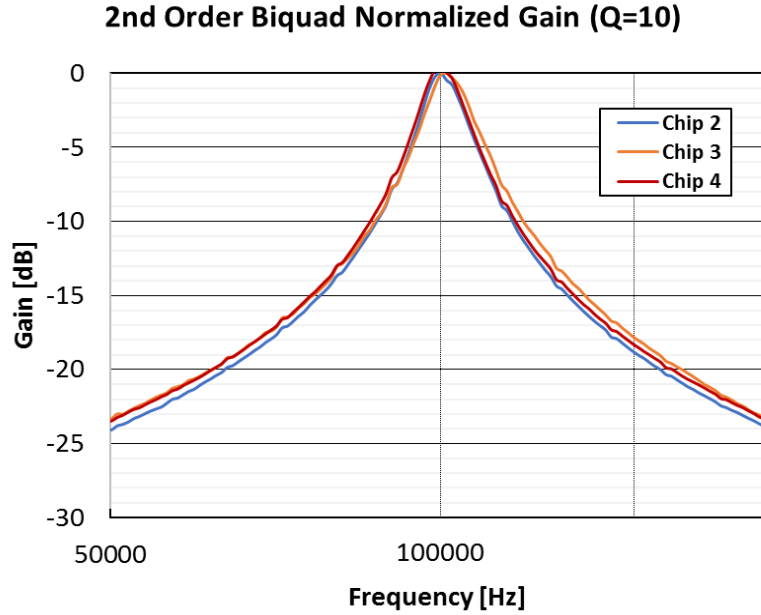


Figure 56: Zoomed 2nd-Order 100kHz MISA2 Biquad Filter of Three Chips

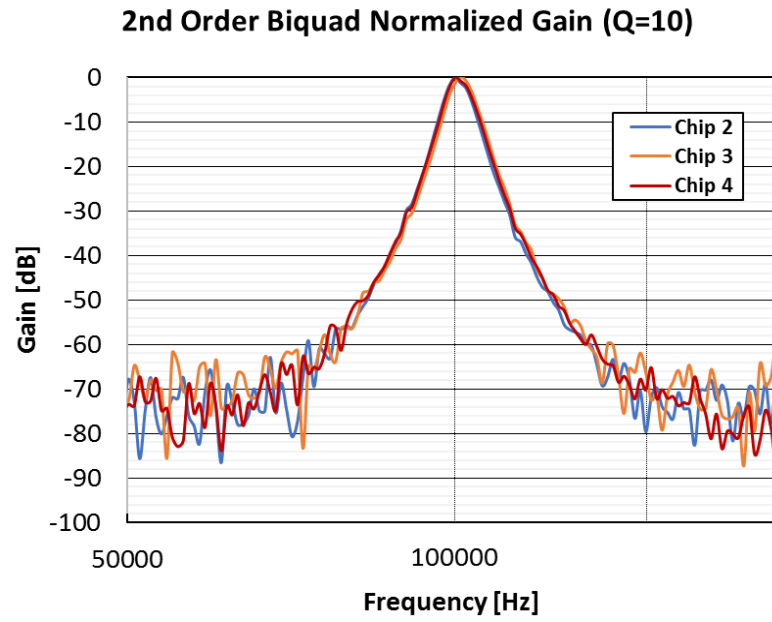


Figure 57: Zoomed 8th-Order 100kHz MISA2 Biquad Filter of Three Chips

The bias current, which sets the filter characteristics, was measured to compare the process variation and mismatch for the biquad filters. The bias current for each of the settings in linearly adjusted as the frequency increases. Figure 58 shows the programmed bias current for G_{m1} and G_{m2} , which set the center frequency, for three different chips. This same biquad current measured on the same chip, but for several different biquad filters in Figure 59. This bias current measurement is repeated for G_{m3} , which sets the Q , for three chips, Figure 60, and four Biquads on the same chip, Figure 61. Finally, the bias current for G_{m4} , which sets the gain of the filter, was measured. Figure 62 display this result for three chips, Figure 63 shows the four Biquads on the same chip. The results here matched reasonably well. Process variation across chips is expected, but the 1kHz bias current can sometimes be quite different than expected.

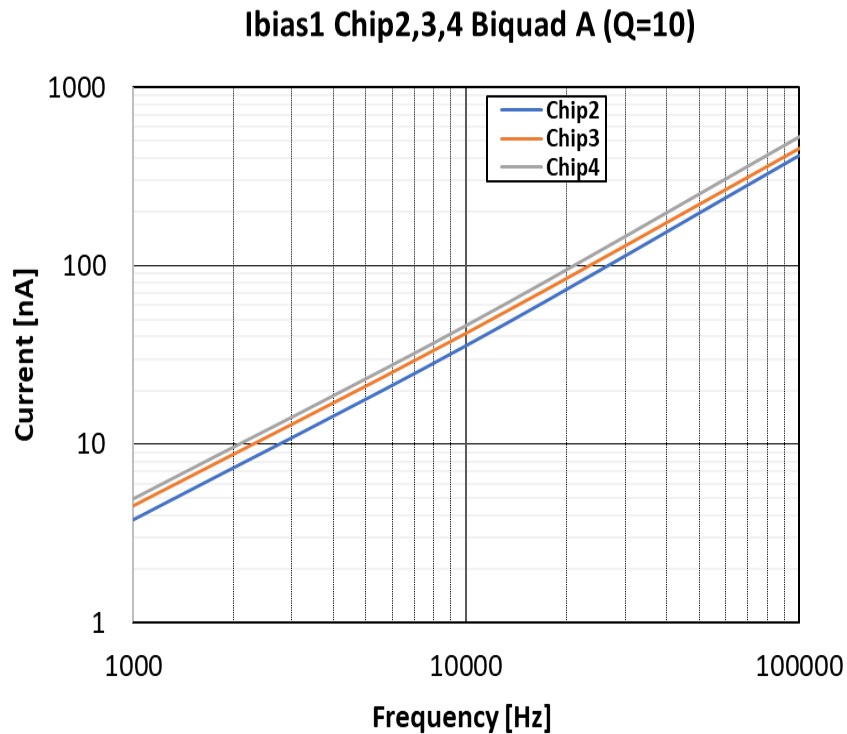


Figure 58: Frequency-Controlled Current Bias for $Q=10$ of Three Chips

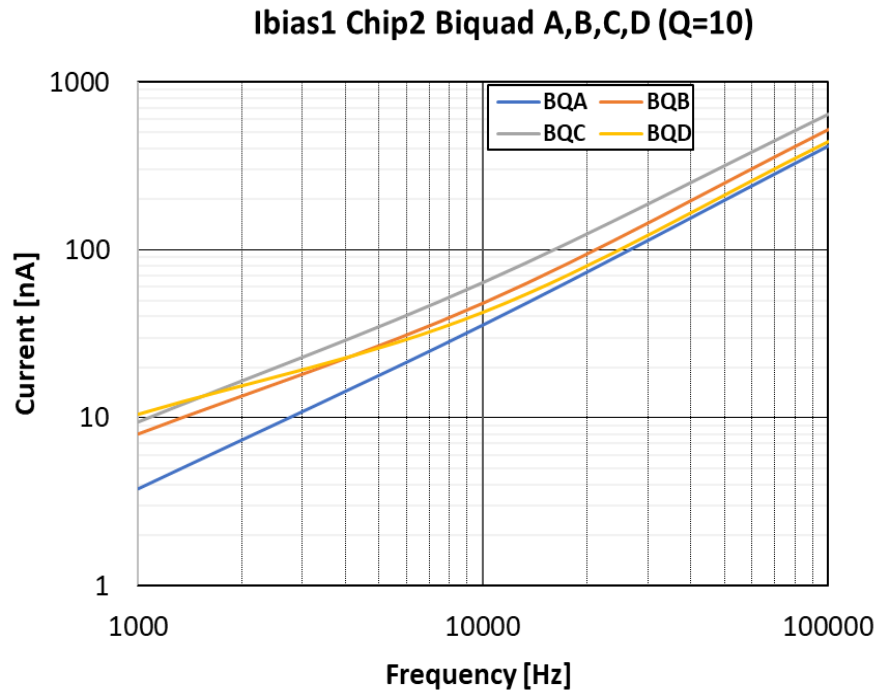


Figure 59: Frequency-Controlled Current Bias for Q=10 of Four Individual Biquads on Chip2

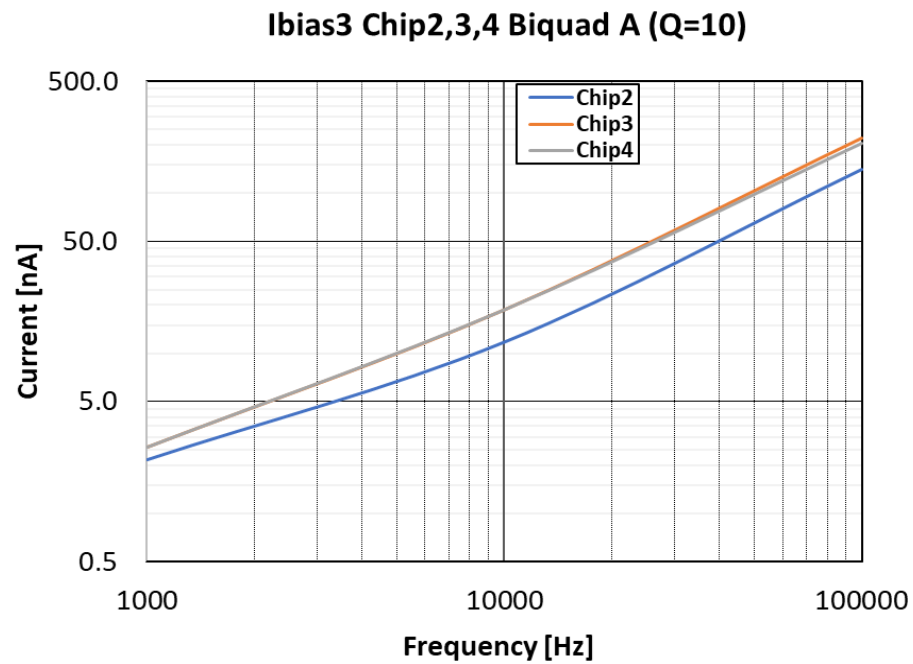


Figure 60: Q-Controlled Current Bias for Q=10 of Three Chips

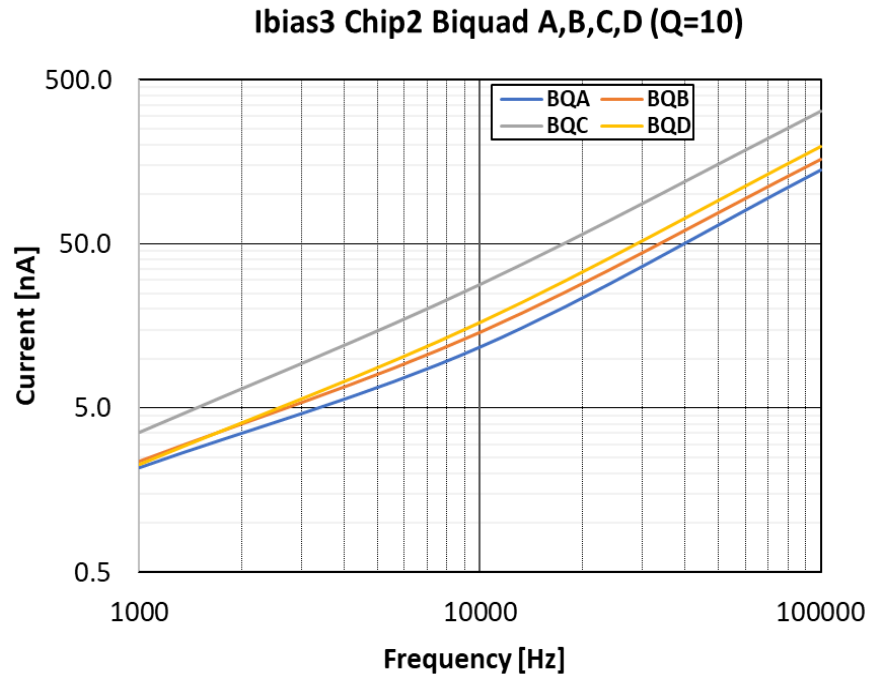


Figure 61: Q-Controlled Current Bias for Q=10 of Four Individual Biquads on Chip2

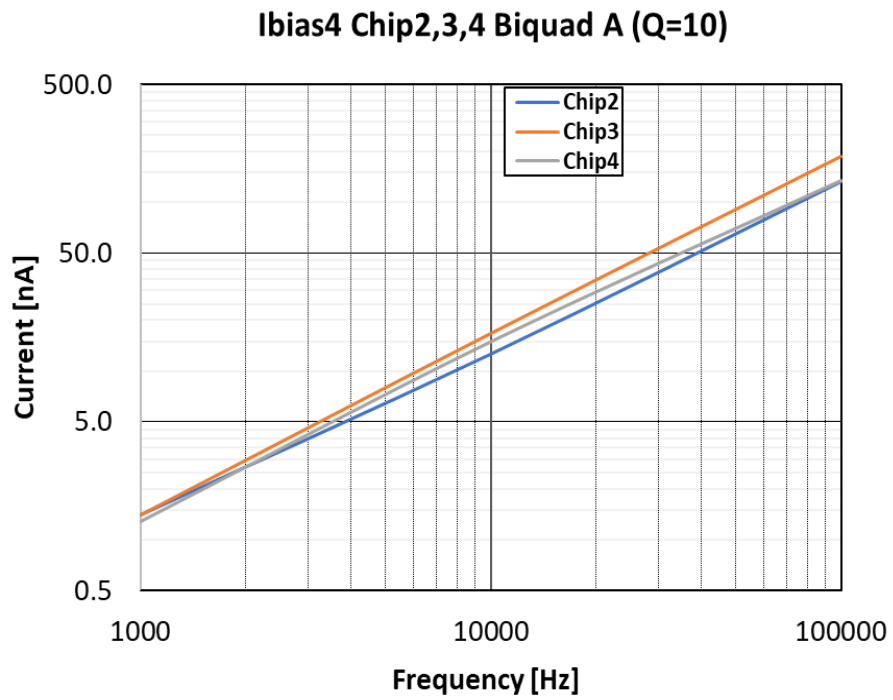


Figure 62: Gain-Controlled Current Bias for Q=10 of Three Chips

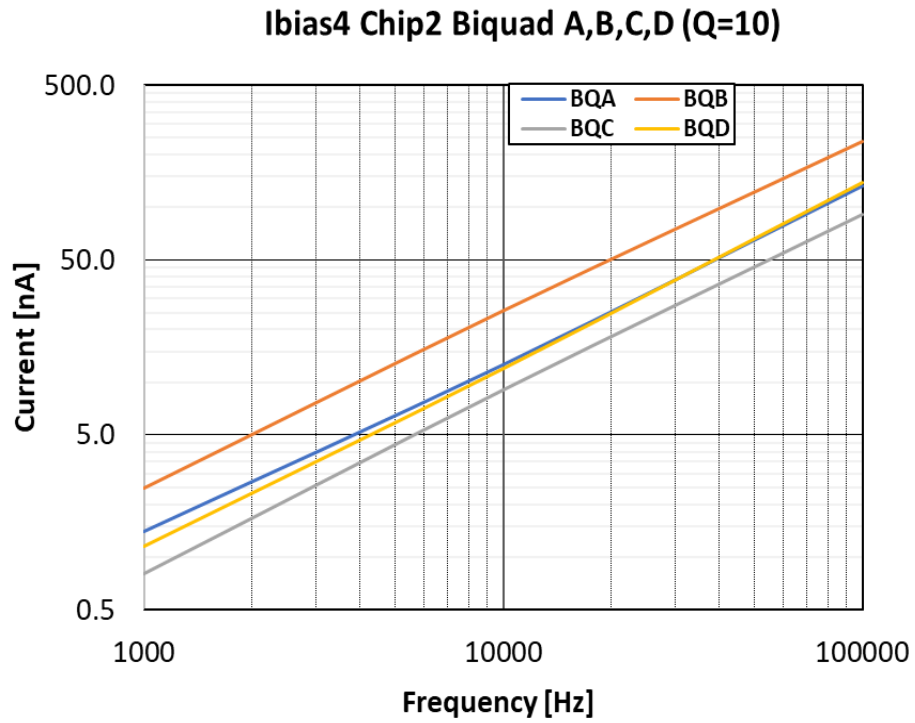


Figure 63: Gain-Controlled Current Bias for Q=10 of Four Individual Biquads on Chip2

CHAPTER FIVE

CONCLUSIONS

Summary of Performance

The MISA2 chip was fabricated in a 180-nm, 1.8V, CMOS process and met or exceeded most of the design requirements. The filter characteristics were capable of being programmed well beyond the required specifications. The biquad center frequency was programmed from 1kHz to 100kHz and operated to frequencies exceeding 500kHz. The quality factor was tunable up to 20, and further if necessary. The filter gain was sufficiently adjustable to maintain a constant 0dB gain at all center frequency and Q settings tested. An 8th-order response was also achieved with individual biasing of biquad filter cells. Power consumption was reduced below the 155 μ W goal for an 8th-order channel. These results support the suitability of this technology for remote sensing platforms used in IoT applications.

Discussion

While most project goals were met with MISA2 design, there are several areas that could be improved. Primarily, the matching of currents in the shared bias channel led to the lack of higher-order measurements in that section. Without the ability to individually program some of the biquad filter cells, no 8th-order transfer function would have been obtained at filter Q values much more than 2. This emphasizes the importance of either much improved matching for shared bias filters or increased support circuitry for individually programmed filters. In response to this issue, another chip (MISA2-1), was recently submitted for fabrication

through MOSIS. This chip should improve the matching performance of the Minch current mirror by significantly increasing the device minimum channel length (4 μ m) enabling shared bias, 8th-order biquad filter bank implementation at Q values > 10.

A couple of other issues with this design were noted. The linear dynamic range was limited to 70mVpp due to either the differential linear input range of the OTA or possibly the internal voltage gain within the biquad filter due to the capacitor ratio. In addition, the performance of the biquad at low center frequencies (1kHz setting) was very sensitive due to the low current bias levels at this setting. Addressing these two issues will further enhance the performance of future MISA-based filter systems.

However, the improvement of the biquad filter is very promising compared to the MISA1 16th-order response. The spectral selectivity is significantly improved over that of MISA1 using only two or three higher Q stages. This means a higher performance filter can be obtained for even less power consumption than before.

Future Work

There are several areas of future improvement for the biquad filter: current matching, low frequency performance, and improved linear dynamic range. The current mirror matching improvement will enable realization of a higher-order filter with less supportive resources necessary and should resultantly improve the power efficiency. An investigation of the 1kHz setting is needed for consistent performance of the filter at lower frequencies and may involve improved filtering. Finally, researching of methods is needed to improve linear dynamic range of the filter enabling improved filter channel signal to noise performance.

Other areas of continued research may involve the optimization of high-order filters and supportive resources, and integration of this system to create miniature, low-power, remote sensing platforms.

LIST OF REFERENCES

- [1] Roehrs, Benjamin David, "A Sub-Threshold Low-Power Integrated Bandpass Filter for Highly-Integrated Spectrum Analyzers. " Master's Thesis, University of Tennessee, 2017.
https://trace.tennessee.edu/utk_gradthes/4775
- [2] Uhrmann H., Kolm R., Zimmermann H. (2014) Gm-C Filters. In: Analog Filters in Nanometer CMOS. Springer Series in Advanced Microelectronics, vol 45. Springer, Berlin, Heidelberg
- [3] R. Chawla, D. W. Graham, P. D. Smith and P. Hasler, "A low-power, programmable bandpass filter section for higher-order filter-bank applications," *2005 IEEE International Symposium on Circuits and Systems*, Kobe, 2005, pp. 1980-1983 Vol. 3.
- [4] B. Rumberg and D. W. Graham, "A Low-Power and High-Precision Programmable Analog Filter Bank," in *IEEE Transactions on Circuits and Systems II: Express Briefs*, vol. 59, no. 4, pp. 234-238, April 2012.
- [5] R. L. Geiger and E. Sánchez-Sinencio, "Active filter design using operational transconductance amplifiers: A tutorial," in *IEEE Circuits and Devices Magazine*, vol. 1, no. 2, pp. 20-32, March 1985.
- [6] Y. Sundarasaradula and A. Thanachayanont, "A 1-V, 6-nW programmable 4th-order bandpass filter for biomedical applications," *2015 IEEE 13th International New Circuits and Systems Conference (NEWCAS)*, Grenoble, 2015, pp. 1-4.
- [7] C. Duan and W. Li, "A 46MHz Biquad Gm-C High Q Bandpass Filter Design for Wireless Application," *2011 IEEE Ninth International Conference on Dependable, Autonomic and Secure Computing*, Sydney, NSW, 2011, pp. 69-72.

- [8] H. Martínez, E. Vidal, A. Cantó, A. Poveda and F. Guinjoan, "Bandwidth-enhancement gm-C filter with independent ω_O and Q tuning mechanisms in both topology and control loops," *Proceedings of 2010 IEEE International Symposium on Circuits and Systems*, Paris, 2010, pp. 3625-3628.
- [9] D. M. Binkley, "Tradeoffs and Optimization in Analog CMOS Design," 2007 14th International Conference on Mixed Design of Integrated Circuits and Systems, Ciechocinek, 2007, pp. 47-60.
- [10] B. A. Minch, "A low-voltage MOS cascode current mirror for all current levels," *The 2002 45th Midwest Symposium on Circuits and Systems, 2002. MWSCAS-2002.*, Tulsa, OK, USA, 2002, pp. II-53.
- [11] Sooch, Navdeep S. High Swing CMOS Cascode Current Mirror. US Patent 4583037, filed August 23, 1984, and issued April 15, 1986.
- [12] H. G. Momen, M. Yazgi and R. Kopru, "A low loss, low voltage and high Q active inductor with multi-regulated cascade stage for RF applications," 2015 IEEE International Conference on Electronics, Circuits, and Systems (ICECS), Cairo, 2015, pp. 149-152.
- [13] D. M. Binkley, B. J. Blalock, and J. M. Rochelle. 2006. Optimizing Drain Current, Inversion Level, and Channel Length in Analog CMOS Design. *Analog Integr. Circuits Signal Process.* 47, 2 (May 2006), 137-163. DOI=<http://dx.doi.org/10.1007/s10470-006-2949-y>
- [14] P. M. Furth and H. A. Ommani, "Low-voltage highly-linear transconductor design in subthreshold CMOS," *Proceedings of 40th Midwest Symposium on Circuits and Systems. Dedicated to the Memory of Professor Mac Van Valkenburg*, Sacramento, CA, USA, 1997, pp. 156-159 vol.1.

- [15] D. De Dorigo, S. Rombach, M. Maurer, M. Marx, S. Nessler and Y. Manoli, "Q-enhancement of a low-power gm-C bandpass filter for closed-loop sensor readout applications," 2015 IEEE International Symposium on Circuits and Systems (ISCAS), Lisbon, 2015, pp. 678-681.
- [16] Vittoz, E.A. & Wang, Alice & H. Calhoun, Benton & P. Chandrakasan, Anantha. (2006). Analog Circuits in Weak Inversion. 147-166. 10.1007/978-0-387-34501-7_8.
- [17] E. J. Kennedy, Operational Amplifier Circuits: Theory and Applications, 1st ed. Holt, Reinhart and Winston, Inc., 1988.
- [18] R. C. Jaeger and T. N. Blalock, Microelectronic Circuit Design, 4th ed. McGraw-Hill Education, 2011.

VITA

Gavin Benjamin Long was born in Knoxville, TN on December 22nd, 1993. He was raised in Greeneville, TN by his parents Todd and Betsy Long. As a member of the Boy Scouts of America, he eventually earned the award: Eagle Scout in December 2011. His high school diploma was earned from Chuckey-Doak High School in May 2012. He attended the University of Tennessee, Knoxville and received his bachelor's degree in electrical engineering on May 2016. During this time, he also interned at Oak Ridge National Laboratory conducting safety classification of electrical equipment and research for an ultrasonic dryer prototype.

Gavin accepted an offer to attend graduate school at the University of Tennessee and participate as a graduate teaching assistant and research assistant under Dr. Benjamin Blalock in the Integrated Circuits and Systems Laboratory research group. While pursuing a master's degree in electrical engineering, he also worked alongside Dr. Nance Ericson and Dr. Charles Britton at Oak Ridge National Laboratory to complete the degree research requirements.